

## CHAPTER 6. STATIC RESERVOIR MODEL

*Martin K. Dubois, Geoffrey C. Bohling, and Alan P. Byrnes*

*For detailed documentation on the construction of the static model see digital appendix: Geomod4\_build*

### INTRODUCTION

Building an accurate static model for the entire Hugoton field (Hugoton and Panoma in Kansas and Guymon-Hugoton in Oklahoma) was the primary objective in the Hugoton Asset Management Project (HAMP). The goal was to develop a model with sufficient detail to represent vertical and lateral heterogeneity at the well, multi-well, and field scale, which could be used as a tool for reservoir management. This required that the model be finely layered (169 layers, 3-ft (1 m) average thickness), and have relatively small XY cell dimensions (660x660 ft, 200x200m; 64 cells per mi<sup>2</sup>). These criteria resulted in development of a 108-million cell model for the 10,000-mi<sup>2</sup> (26,000-km<sup>2</sup>) area modeled. Although lithofacies geo-bodies tend to be laterally extensive, covering multi-section to township scales, small XY-cell dimensions were required to allow the extraction of portions of the model for local reservoir simulation. The Hugoton geomodel may be the largest model of its kind (lithofacies-controlled, property-based water saturations), and the workflow illustrates how very large models can be built.

The simplified workflow presented in Figure 6.1 might be interpreted to indicate that the workflow process was linear; however, it is important to note there are multiple feedback loops at varying scales (with each step, between adjacent steps, and involving multiple steps). In addition, there were multiple iterations in the workflow at scales from individual steps to the model scale. At the model scale, there were four major iterations, Geomod1 through Geomod4. Geomod1, prior to HAMP, was a model for the Council Grove in Kansas where the basic workflow strategy was developed (lithofacies defined in core, lithofacies predicted in non-cored wells with neural networks trained on core, core and wire-line log petrophysical properties tied to lithofacies, and property-based water saturations), and automated processing tools were prototyped (Dubois et. al., 2003). Geomod2 covered a relatively small area around the Alexander D simulation area (see Chapter 9) and was the first model that included the Chase. It used neural networks to predict lithofacies from wireline-log response and petrophysical transforms from Council Grove to predict properties in the Chase. After Chase core lithofacies and petrophysical data were added to the dataset, the next generation of models were developed (Geomod3), first for two 70-mi<sup>2</sup> models in the Flower (Stevens County) and Graskell (Grant-Haskell County line) areas (see Chapter 9) and then for the full field. Geomod3 was the basis for the paper presented at the 2006 American Association of Petroleum Geologists core workshop on modeling giant reservoir systems and for Dubois et al. (*in press*). Geomod4, the latest model, included more core (doubled from 14 to 28 wells) and more model “node” wells (1364 to 1600 wells) than did Geomod3, but the resulting models were remarkably similar.

Each iteration of the model included successive generations of neural network training, refinement of core petrophysical property algorithms, wire-line log property corrections, and improvements to the automation process. It is noteworthy that successful deployment of the multi-iteration strategy was possible only through very close and ongoing integration of work by six scientists (from multiple disciplines) at the Kansas Geological Survey and three consultants over a 2-1/2 year period. Concurrent with model building, numerical simulations of dynamic models of portions of the larger geomodel were conducted to validate the static model process (Chapter 9). History-matched simulations served to ground truth the model at the well to multi-well scale, which was critical to building confidence in the modeling process and the static model as an accurate model of lithofacies, petrophysical properties, water saturation, and gas in place. Although the multiple-iteration-model strategy might seem inefficient compared to a more linear approach (gather all data, analyze all data, model all data), this approach proved very effective for many reasons: 1) enabled adjustment in the approach after discovery of new knowledge (e.g., Chase and Council Grove behave as a common reservoir rather than as separate reservoir systems), 2) allowed critical tactical decisions to be made early in the process (e.g., lithofacies class boundaries and number of lithofacies), 3) facilitated participation and technical review by industry partners, and 4) enabled early results to be disseminated to industry partners for their immediate use.

### **Static Model Accuracy**

The accuracy and utility of the Hugoton geomodel can be measured by several metrics including prediction accuracy of parameters like lithofacies, petrophysical properties, and OGIP at the well- to field-scale. The only direct measure for lithofacies is the comparison of predicted- and core-defined lithofacies. We can also qualitatively measure the validity of the lithofacies model by 1) comparing it with earlier work at smaller scales, and 2) comparing the three-dimensional lithofacies patterns with depositional models that have been proposed for the area and for upper Paleozoic cyclic depositional systems in general. Measures of accuracy for any parameter at the lease and field scale are constrained by lack of data measured at this scale and the need to compare parameters, such as OGIP. However, OGIP estimation requires integration of many parameters, the product of which may be inaccurate due to error in a single parameter or improper integration of accurate parameters due to improper scaling of properties or the input of a property that was not modeled. Ultimately, measures of accuracy and utility of a geomodel at the lease and field scales are often defined by comparison of predicted and measured production and pressure history, where the predicted pressure and production data are obtained from input of the static geomodel (the focus of this paper) into a reservoir flow simulator to obtain a dynamic model. The workflow involved in calibration of the geomodel with dynamic data is not shown in Figure 6.1 but was an important part of testing and refining the geomodel. Dynamic modeling has been performed on one 9-square-mile and two 12-square-mile areas (23 and 31 km<sup>2</sup>), including histories for 28, 39, and 15 wells, respectively, to test and refine the geomodel discussed here (see Chapter 9). These simulations generally validate the present geomodel but show

how uncertainty in some properties (e.g., free-water level) must be reduced to optimize the model accuracy for use in predicting field performance.

## 6.1 WORKFLOW

*Martin K. Dubois and Alan P. Byrnes*

The general workflow for developing the Hugoton geomodel shown in Figure 6.1 can be characterized as comprising four principal steps: 1) Compile data for stratigraphy (formation tops) and core lithologic properties, petrophysical properties, wireline logs, fluid properties, and production and analyze data to certify that the data meet quality and accuracy criteria; 2) Define properties/develop algorithms comprising training a neural network and predicting lithofacies at node wells and developing wireline-log analysis algorithms (including corrections) and petrophysical properties algorithms (e.g., permeability-porosity ( $k-\phi$ ), capillary pressure ( $P_c$ ), relative permeability( $k_r$ )), 3) Develop databases of properties for use in geomodel construction including lithofacies, porosity, tops, free-water level at node wells, and 4) Develop geomodel by constructing 3-D cellular model using tops database, populating node-well cells with lithofacies and porosity database properties, upscaling properties as appropriate and populating 3-D model with basic properties, then utilizing petrophysical algorithms, populate 3-D cellular model with lithofacies-specific petrophysical properties and fluid saturations.

Several of the components of steps 1 through 3 of the workflow have been described in detail in previous chapters. Compiling and defining lithofacies in core involved detailed analysis at the ½-ft (0.15 m) scale of 6756 ft (2060 m) of core from 28 wells (Chapter 4, section 4.1). Compiling core petrophysical data and developing algorithms for predicting permeability, relative permeability, and water saturation was discussed in Chapter 4, section 4.2. For water saturations to be estimated through capillary-pressure relationships, a free-water level (FWL) must be accurately defined. Chapter 7, section 7.2 discusses how the FWL was estimated for the entire field by using a combination of three indicators: (1) base of lowest perforations; (2) position where log calculated water saturation equals 100% in field pay zones; and (3) calculation of the FWL for an estimated original gas in place (OGIP).

The Hugoton static geomodel was constructed using Petrel™, Schlumberger's reservoir modeling software. For this software and the geomodel constructed basic input data comprise: lithofacies and porosity at half-ft (0.15 m) intervals, well header information to relate porosity and lithofacies to XYZ space, formation-member level tops set, and grids representing seven structural framework horizons and the free-water level. Water saturation and permeability in the XY and Z directions are calculated at the cell level using the lithofacies-specific algorithms developed. Modeling in Petrel™ was accomplished with minimal problems due to extremely meticulous quality control in other applications, primarily in the geologic mapping application Geoplus Petra™. Significantly more time was spent in data compilation and algorithm development than in constructing the geomodel. The following sections discuss important aspects of the workflow that are not been covered in other chapters. Specific elements of the static model that are the focus of this discussion are the construction of the 3-D grid structure, lithofacies model, porosity model, and calculations within Petrel™ for creation of the petrophysical model. These are highlighted in the workflow in yellow (Figure 6.1)

## 6.2 3-D STRUCTURAL/STRATIGRAPHIC GRID MODEL

*Martin K. Dubois*

### Static Model Input Data

#### *Formation/Member tops set and structural framework*

The primary source for structural tops in Kansas was the Kansas Geological Survey database (<http://www.kgs.ku.edu/PRS/petroDB.html>). Tops used were those picked from wire-line logs at the formation or member level (1/2-cycle) by geologists in a five-year industry-supported Hugoton Project (<http://www.kgs.ku.edu/Hugoton/index.html>) that ended in 2003, plus those added by those involved in this study. Tops for Texas County, Oklahoma, were gathered in this study by correlating well logs with the Kansas intervals. Twenty-five tops in all were used in the model (Figure 6.2 and Table 6.1). The set of tops was scrutinized for error by building a series of structure and isopach maps (each formation or member) and visually inspecting them for anomalies. Flagged points were either corrected or eliminated from the dataset. Seven of the 25 tops (Table 6.1) from over 8850 wells (Figure 6.3) were used to build structural framework grids that form the top and base horizons for six separate models. High well density provides very good structural control for the geomodel. The framework horizons were built in Geoplus Petra™, and imported into Petrel™ because we found that contouring algorithms were more satisfactory in Geoplus Petra™. The full compliment of 25 formation or member tops from 1600 “node” wells, wells with lithofacies and porosity, were used to build zones within the structural framework in the Petrel™ models.

#### *Digital well logs*

Digital well logs were critical to the project for lithofacies prediction and porosity and were made available for more than 5000 wells through contributions by industry participants in the project. These were combined with those from the Kansas Geological Survey database (approximately 1000 wells). In this pool of log data, 1600 had the required curves required by the neural-network models (gamma ray (GR), density and neutron porosity (Dphi and Nphi, and deep resistivity (ILD)) and also passed a screening process that eliminated irregular data. Approximately 1000 of the 1600 well log suites included a photoelectric curve (PE). We chose not to normalize or correct curves that were out of normal range, but instead eliminated inappropriate well logs in a rigorous screening process in, Geoplus Petra™. Screening was accomplished through the generation and mapping of selected statistics (mean, range, minimum, maximum) over specific stratigraphic intervals for each curve and eliminating outliers through visual inspection.

#### *Assemble data files for Petrel™*

Once all input data in the tops, lithofacies, and porosity databases were checked for quality assurance, geomodel input files were prepared (Table 6.2). Required input files

include lithofacies and porosity at half-ft (0.15 m) intervals, well-header information to relate porosity and lithofacies to XYZ space, formation-member level tops set, and grids representing seven structural framework horizons and the free water level.

## **Static Model Construction**

The extremely large area (10,108 sq mi), small XY cells (660 x 660 ft) and relatively thin layers (169 layers, 3.3 ft-thick average) resulted in a 110 million-cell model that required subdividing the model into parts due to computational limitations. Because the main pay intervals are separated stratigraphically by intervals with relatively poor reservoir properties and lithofacies and property modeling is restricted by zones in the modeling process, we chose to subdivide the Chase and Council Grove model stratigraphically rather than geographically, with three multi-zone, multi-formation models in the Chase and three in the Council Grove (Figure 6.2). Each of the six models was built with the same starting architecture and layering to facilitate cutting out selected portions of the six models and assembly into smaller models. These have a complete vertical section of the reservoir system but are limited in areal extent and can be more easily managed for further analysis and reservoir simulation. The structural framework for the six models was based on a structural tops database for 8850 wells (Figure 6.3). Our dataset of tops in Oklahoma is less complete than it is in Kansas. Layering within the models used the following hierarchy: 1) division between formation/members, 2) further subdivision between continental and marine intervals, 3) further subdivision into 169 layers based on minimum vertical thickness of the key lithofacies in the node wells. Layers averaged 2-ft thick in the marine intervals and 4-ft thick in the continental intervals. The following sections discuss the population of the 3-D model with lithofacies and with petrophysical properties.

### **6.3 LITHOFACIES ESTIMATION AT WELL TO MODEL SCALE**

*Geoffery C. Bohling and Martin K. Dubois*

#### **Lithofacies Prediction at Node Wells**

Classification of lithofacies and their accurate representation in a 3D cellular geologic model is critical to the project because permeability and fluid saturations for a given porosity and height above free water vary considerably among lithofacies (Dubois et al., 2003). The best source of lithofacies information is core samples of reservoir rock from wells; however, cores are not commonly taken due to the expense. Because the availability of core is limited compared to the number of wells in the field, a method for estimating lithofacies in wells without cores is necessary. In this case, lithofacies from cores are extrapolated from wells with cores (training wells) to wells without core (model node wells) through the comparison of physical rock properties measured by wire-line logs in both the cored wells and wells without cores.

### *Neural network training*

To predict lithofacies using neural-network analysis, we used a standard single-hidden-layer neural network (Hastie et al., 2001) based on wire-line well logs in 1600 node wells throughout the Hugoton and Panoma fields. As illustrated in Figure 6.4, the input vector to the neural network included two computed geologic variables, a depositional environment indicator (MnM) and a stratigraphic cycle relative position (RelPos), in addition to the following wire-line log parameters: gamma ray, logarithm of deep induction resistivity, average of neutron and density porosity, neutron-density porosity difference, and photoelectric factor (PE, where available). No adjustment was made for thin-bed or boundary effects. For each input vector, the network computed a vector of output values representing the corresponding lithofacies membership probabilities, and the most probable lithofacies was assigned for the logged interval. The network was trained based on association between core-defined lithofacies and the log and geologic constraining variables. A comparison of core-defined lithofacies, lithofacies membership probabilities, and predicted discrete lithofacies is shown in Figure 6.5.

The two geologic variables were derived from a 25-formation (or member) set of tops (Figure 6.2), which are also the tops of marine or nonmarine (continental) half-cycles. Values for the depositional environment indicator were 1-nonmarine (continental) and 2-marine, and for the Herington and Holmesville, where intertidal environments dominate, 3- intertidal. The MnM variable helps to distinguish between lithofacies with similar petrophysical properties but developed in different broad depositional environments. Values for the stratigraphic cycle relative-position parameter (RelPos) range linearly with depth from 0 at the bottom of each half-cycle interval to 1 at the top, indicating position within each interval. Including this curve allowed the network to encode information regarding the fairly regular succession of lithofacies succession commonly exhibited within each interval, and thus transfer some of that character to the sequence of predicted lithofacies in each well. The two curves were computed for the node wells using Visual Basic code within an Excel spreadsheet run in a batch-processing routine and exported as log curves in a LAS file format, as described in Chapter 5. They were then combined with the wire-line log curves to complete the feature vector.

The neural network code has been added to Kipling.xls, an Excel add-in for nonparametric regression and classification (Bohling and Doveton, 2000). For this study, the network was trained to match observed associations between logs and lithofacies identified in core from a set of key wells shown in Figure 6.6 (17 Chase wells with 7108 half-ft intervals in the training set, and 16 Council Grove wells with 6404 half-ft intervals). Fundamental parameters controlling the network behavior are the number of nodes in the hidden layer (network size) and a damping or decay parameter. Increasing the network size allows the network to match the training set more closely, but using too many hidden-layer nodes leads to the network becoming precisely tuned to the training data and unable to generalize. Increasing the damping parameter counteracts precise tuning, forcing the network to develop smoother representations of the boundaries between lithofacies.

We used cross-validation to estimate the optimum values for network size and damping parameter. The cross-validation was done in two ways: 1) splitting the entire training dataset, regardless of well, into random subsets, with 2/3 of the cases used for training and the other 1/3 for testing (comparison of predicted and actual lithofacies), and 2) taking out each well in turn, training on the remaining wells, and testing on the removed well. Training and testing were repeated several times for each parameter combination to account for the random variation between different realizations of the network. This computationally intensive cross-validation was performed using scripts in the R statistical computing language (R Development Core Team, 2005) using the *nnet* function developed by Venables and Ripley (2002). The scripts computed several measures of correspondence between actual and predicted lithofacies, including the average lithofacies misallocation cost for all intervals in the test well. This value is computed from a misallocation cost matrix that assigns a cost for misallocation that is proportional to the “distance” in lithofacies code units in the lithofacies spectrum from actual. For example, calling a packstone (L7) a marine siltstone (L3) carries a higher cost than confusing it with a grainstone (L8) with similar petrophysical properties. Absolute accuracy in lithofacies prediction, though desirable, is unrealistic and our goal was to limit error to the nearest lithofacies class. Plots of median average misallocation cost versus damping parameter and network size (panel variable) for the well-by-well cross-validation including the photoelectric wire-line log (PE) in the Council Grove (Figure 6.7) illustrate the median computed over 30 average misallocation costs for each parameter combination: five trials per well for each of the six Council Grove wells with PE logs. Cross-validation plots for the Council Grove case without PE and for the Chase, with and without PE were similar (not illustrated). Although the network performed reasonably well over a range of parameter values, we chose to use a network size of 20 hidden layer nodes and a damping parameter of 1.0. The damping parameter chosen (1.0) exhibited consistently low misallocation values and the number of hidden layer nodes (20) was chosen over configurations with fewer nodes that tended to over-generalize.

Initially, we trained four neural networks: Chase with and without PE logs and Council Grove with and without PE logs. Predictions using the model including PE were used wherever possible. The Chase models included all 11 lithofacies, but the Council Grove models included only 10, because the fine- to medium-crystalline dolomite does not occur in the Council Grove in sufficient volume to be considered as a separate class. In the latest modeling iteration (version Geomod 4), we added two additional models and split the stratigraphic section slightly differently. The uppermost model covered the upper part of the Chase, from the Herington to the top of the Fort Riley. The Fort Riley and Matfield were modeled together, and the Wreford, the lowermost zone of the Chase, was modeled with the Council Grove. An additional variation in the latest modeling was the use of “recruits” in order to increase the number of samples in the training for the phylloid algal bafflestone and marine sandstone in the Council Grove. For these lithofacies we “harvested” log curves from intervals in wells near the cored wells where we were certain of the lithofacies and included them in the training set. These six neural network models were then applied as appropriate to produce predicted lithofacies versus depth logs at half-ft intervals in the 1600 node wells distributed throughout the field (Figure 6.3). The batch-prediction capability of the Kipling program was used in this

case, with logs being read from LAS files and the predicted lithofacies curves being written out to LAS files.

### ***Lithofacies prediction***

After digital wire-line log curves and formation or member tops were gathered and prepared, and neural networks trained on core-defined lithofacies, the next step was to predict lithofacies at the ½-ft scale (0.15 m) in wells with appropriate log curves. Below are the steps involved in predicting lithofacies using neural networks:

1. Alias log curves to a common name. Curves required are gamma ray, density and neutron porosity, and deep resistivity. Photo-electric curve is optional, but improves accuracy.
2. Generate geologic-constraining variables including relative position to base of ½ cycle (RelPos) and marine-nonmarine (MnM) using an automated process. Output is in a Log ASCII Standard (LAS) file format.
3. Generate log-curve predictor variables: gamma ray (API units), natural logarithm of the deep resistivity (lnILD), difference between neutron and density porosity (Nphi-Dphi), average of neutron and density porosity ((Nphi+Dphi)/2) and photoelectric effect (PE), if available.
4. Create LAS formatted files, one per well, which includes the four or five log variables (in step 3) and MnM and RelPos curves and export files from multiple wells, placing them in a single file folder.
5. Use Kipling.xla (Bohling and Doveton, 2000) neural-network module batch-prediction option to predict lithofacies after choosing the appropriate, trained neural network.

As part of the quality-control process, lithofacies estimated by the trained neural networks were then imported into and checked in Geoplus Petra™ for problems by mapping a variety of lithofacies statistics in 2-D maps. This same process was part of the iterative process to optimize the neural network training.

### **Estimate Lithofacies in Cellular Model**

Following construction of predicted lithofacies-depth curves, the predicted lithofacies curves were read into Petrel™ (Schlumberger 3-D modeling software), and upscaled to the resolution of the model layers (roughly 2 ft in marine intervals and 4 ft in non-marine intervals) by “majority vote”: the lithofacies for each model cell intersecting a well is taken to be the most frequently occurring lithofacies in that layer in the well. Voxel-based methods were chosen over object-based methods for lithofacies and property modeling due to the relatively dense well control and geometry of the lithofacies bodies being modeled (thin and laterally extensive). Sequential indicator simulation (Deutsch and Journel, 1998) as implemented in Petrel™ was used to generate lithofacies values in all model cells using vertical proportion curves generated with the application’s data analysis tool, and conditioned on the upscaled lithofacies values in the node well cells. Likewise, corrected porosity curves were also read into Petrel™ and upscaled using

arithmetic averaging. Porosity values over the entire model were generated using sequential Gaussian simulation (Deutsch and Journel, 1998). Both of these stochastic simulation procedures require the specification of a variogram model for each lithofacies describing the spatial correlation behavior of the property being simulated.

### *Variogram Analysis*

Developing variogram models for two properties (facies occurrence and porosity) for three spatial directions, 11 lithofacies, and 24 zones – a potential total of 1584 variograms – is a daunting task and required some simplification and automation to be made tractable. Automation was accomplished by exporting the upscaled lithofacies and porosity values at the wells from Petrel™ and reading them into the R statistical computing environment for automated processing, rather than using the interactive variogram analysis tools in Petrel™. Simplification consisted of computing only one variogram per lithofacies for each of the six different sub-models, rather than for each of the 24 zones, and imposing certain restrictions on the form of the variogram models – namely, using an exponential variogram model with zero nugget and horizontal isotropy (same range in all horizontal directions), reducing the model parameters to be estimated to the variogram sill, vertical range, and horizontal range. This reduced the potential number of variograms to 264.

Although the automation and simplification made the variogram modeling process more manageable, it did not eliminate interpretational difficulties caused by non-ideal behavior of the empirical variograms, computed from the upscaled data at the wells. Prior to analysis, both the lithofacies data and the porosity data are subjected to scalings that should result in variogram sills, reflecting the global variance value, of 1. However, many of the computed variograms, particularly those in the horizontal direction, failed to reach a sill of 1.0. This is probably due in part to zonal anisotropy (Deutsch, 2002), meaning that the full range of variability (used in the scaling process) is not seen when examining data from vertically limited windows along the horizontal direction. This causes complications in variogram fitting because a sill of 1.0 is enforced on the model variogram, meaning that the model variogram cannot possibly match the empirical variogram in this case. In addition, many of the horizontal variograms exhibit higher nuggets, reflecting short-scale variability, than we are willing to use in the model variogram. Use of a high nugget in the variogram model causes the simulated lithofacies and porosities to be very noisy or patchy, a behavior that we do not believe reflects reality, despite the high nuggets in the empirical variograms. In theory, the horizontal and vertical variograms should share the same nugget value. It is common practice to weight the vertical variogram more heavily in the nugget estimation, because the vertical variogram is generally derived from dense, regularly sampled data and therefore reflects short-scale variation more accurately. In this case, we have taken the extreme measure of enforcing a zero nugget in all cases, a decision that is at least not too strongly contradicted by the vertical variograms. However, this means that the fitted variogram models do not match the apparent nuggets in the empirical horizontal variograms in many cases.

### *Lithofacies variograms*

For each of the six submodels, the upscaled lithofacies and porosity values at the wells were exported from Petrel™ to a GSLIB-format ASCII data file. These data files were then read into the R statistical analysis package for processing with the Gstat package (Pebesma, 2004). A set of R-language scripts was developed to compute the empirical lithofacies occurrence variograms in both the vertical and horizontal directions, by lithofacies for each submodel, and fit an exponential variogram model to the empirical variogram, as long as there was adequate data to estimate the empirical variogram for that lithofacies and submodel. For a binary variable like lithofacies occurrence, the global variance should be given by  $p*(1-p)$ , where  $p$  is the global proportion of the lithofacies in the dataset being considered. Thus, scaling by  $p*(1-p)$  should yield an empirical variogram with a sill of 1.0. As mentioned above, this was not the case for many of the lithofacies variograms. In an attempt to reduce the effects of zonal anisotropy, the variogram computation scripts employed here actually apply this scaling on a layer-by-layer basis and then average the scaled variograms for all the layers to obtain a variogram for the entire submodel. The reasoning behind this is that a lithofacies proportion,  $p$ , estimated for each layer, should provide a more appropriate scaling for that layer than a lithofacies proportion estimated from the entire dataset. This process did seem to reduce the zonal anisotropy problems relative to the globally scaled variograms, but did not eliminate those problems.

With the imposed constraints on the model form – an exponential model with a zero nugget – the model-fitting process was reduced to estimating the vertical and horizontal ranges. Figure 6.8 shows the empirical vertical variograms for lithofacies five for all six submodels, along with the fitted exponential models. Again, the model sill of 1.0 is enforced by theory (and by Petrel™). Overall, these fits are not bad and the decision to enforce a nugget of zero does not cause significant difficulties. The hints of oscillatory behavior in the empirical variograms for a few of the submodels are not surprising, because one expects to see oscillations in a variogram describing a property displaying cyclicity. These results are reasonably typical of vertical variograms for all lithofacies. Note that a maximum value of 25 ft was imposed on the fitted vertical ranges and range estimates for some badly behaved empirical variograms did reach this upper limit, essentially indicating an inability to obtain a reasonable fit.

Figure 6.9 shows the set of horizontal empirical variograms for lithofacies 5, along with the fitted models. These empirical variograms display the typical problems: high nuggets and sills less than 1.0. The resulting fits are also typical of the horizontal fits for all lithofacies. The fit for the Winfield-Fort Riley interval (WinFtRiley) is almost reasonable, although clearly not perfect. The fitted horizontal range in this case is 11,500 ft. The fitted range for the B2LM-B4LM interval is very short, 3700 ft, to fit an empirical variogram that is almost pure nugget. (A pure nugget model would describe a process that is purely random in space, displaying no spatial autocorrelation.) The fitted range Fort Riley-A1SH interval, 42,000 ft, is much larger than we expect, approaching the imposed maximum fitted range of 50,000 ft. This fit is essentially meaningless,

reflecting the inability to match the observed variogram under the imposed model constraints.

### ***Applying variogram analysis results in the model***

The fitting exercise described above resulted in a very large tabulated set of estimated vertical and horizontal ranges for lithofacies occurrence and porosity for all 11 lithofacies in all six submodels (three in the Chase and three in the Council Grove) having sufficient data for a given lithofacies. A qualitative evaluation of the quality of the fit, which ranged from good to meaningless (for cases where the fitted model failed to match the empirical variogram at all – often cases where the range estimate reached the imposed upper limit of 25 ft in the vertical or 50,000 ft in the horizontal) was assigned to the ranges for each variogram analysis. These data were then combined by group (Chase or Council Grove) or by combined groups (Wolfcamp) in the cases where there were not sufficient data at the group level, in summary tables (Tables 6.3 and 6.4). Fitted ranges by individual submodels were not used, but were instead generalized for different combinations of intervals and lithofacies. In cases where there were sufficient data, mean values for ranges by lithofacies by group (Chase or Council Grove) were calculated and implemented in the modeling. Where there were insufficient data by group (Chase or Council Grove, separately), but sufficient when the data were combined, then mean ranges for the combined groups (Wolfcamp) were calculated and implemented in the modeling. For lithofacies where ranges could not be estimated from the analysis, ranges from adjacent lithofacies were generally used. Ranges of 50,000 or greater were not considered. Tables 6.3 and 6.4 generally describe the variograms used for version Geomod 4. Slightly different major and minor axis for marine lithofacies results in elliptical ranges. We have no quantitative data to support the choice to establish a slight bias with an azimuth for lithofacies. However, there is a tendency for lithofacies geobodies to trend parallel to the depositional strike (north 11 degrees east) in the models constructed, so a slight bias was used during modeling. For details see digital appendix *Geomod4\_variograms*.

## **6.4 LITHOFACIES DISTRIBUTION IN THE STATIC MODEL**

*Martin K. Dubois*

Lithofacies and property distributions in the 3-D Hugoton cellular geomodel presented are consistent with earlier work on the Hugoton (Garlough and Taylor, 1941; Hubbert, 1953; Pippin, 1970; Parham and Campbell, 1993; Fetkovitch et al., 1994; Oberst et al., 1994, Seimers and Ahr, 1990; Olson et al., 1997; Heyer, 1999; Sorenson, 2005), although the present model covers a larger scale at a finer resolution than these studies. The full-field geomodel presented here reveals lithofacies and property patterns that could not be identified at smaller scales. Figures 6.10 to 6.19 are a series of cross sections and map views of lithofacies and properties for the six individual models. General trends in thickness and lithofacies distribution are evident in the 3-D volume: continental rocks are thickest and marine carbonate intervals thin or pinch out at Hugoton's western updip margin and the relationship is nearly reciprocal basinward. The important reservoir

lithofacies (grain-supported carbonate, dolomite, marine and continental sandstone) are laterally extensive and the marine carbonates, the primary pay zones, are separated by laterally continuous continental siltstone with poor vertical transmissibility.

### **Quantitative Measures of Lithofacies at Varying Scales**

Quantitative measures of lithofacies proportions (Table 6.5) in core, neural network predicted lithofacies at node wells, upscaled at the node wells and in the 108 million-cell model, show consistency at the different scales, suggesting that the sample rate for training and lithofacies prediction in each of the three steps was sufficient. Slight variations in the measures are likely to be related to sample distribution in core versus the node wells and the increase in scales from 0.5 ft (0.15 m) to considerably thicker cells (layers). A number of factors related to the nature, geometry and distribution of the predicted lithofacies and the variables chosen to predict lithofacies are believed to have enabled the success of the neural networks in predicting lithofacies at the node wells and the modeling of lithofacies between nodes. Lithofacies classes were chosen to maximize differences in the signature of wire-line log variables. Geologic constraining variables (e.g., relative position curve and marine-nonmarine curve) captured and leveraged geologic information such as the predictable vertical succession of lithofacies in the sedimentary cycles and primary depositional environment. The extensive lateral continuity of the lithofacies, with typical lithofacies-body sizes much larger than the lateral spacing between node wells, contributed to the success of the sequential indicator simulation of the lithofacies distribution. Significantly, adequate core control enabled appropriate sampling of the reservoir system for the lithofacies training set. Without core, the model could not have been built.

The most common misallocations of lithofacies were prediction of grainstone (L8) as wackestone or packstone (L5 and L7), predictions of carbonate mudstone (L4) as wackestone (L5), and predictions of the continental sandstone (L0) as coarse siltstone (L1). These incorrect lithofacies predictions reflect overlaps of the log characteristics of the lithofacies. Fortunately, the lithofacies involved are also sufficiently similar in their petrophysical properties that the resulting distributions of porosity, permeability, and water saturation resulting from random misallocations were not significantly different from correct properties distributions, discussed in Chapter 4, section 2.

The “majority vote” upscaling of lithofacies from the half-ft sampling interval to the thickness of the model layers intersecting each well did not significantly alter the lithofacies populations. Using this methodology we would not expect to see a significant difference in lithofacies populations unless certain lithofacies typically occurred in thin bodies separated by fairly large vertical intervals, resulting in a systematic under-representation of those lithofacies in the upscaled results. Finally, the lithofacies proportions in the full 3-D model closely reflect those for the upscaled well cells. This is not surprising, because the stochastic indicator simulation attempts to match the proportions observed in the conditioning data. The distribution of our node wells was

sufficiently uniform such that the lithofacies proportions in the conditioning set were very similar to those in the reservoir system.

### **Lithofacies Distribution in the Model**

Large-scale sedimentation patterns, interpreted from lithofacies distribution, are striking when viewed at the scale made possible by the full field-scale model. In cross section at the inter-cycle scale, back-stepping of major lithofacies associated with changes in water depth and energy are evident in the Chase marine carbonate (Figure 6.10), particularly in the two dolomite lithofacies. The position on the shelf where continental siliciclastics thicken at a higher rate also back-steps in a similar manner. Marine carbonates in the middle three of the seven Council Grove cycles (Figure 6.10C) pinch out at the western field margin. The gradual shift in the paleo-shoreline position, first to lower on the shelf and then back to a higher position, is believed to be related to a change in sea level amplitude. The symmetry demonstrated by sedimentation patterns around the middle cycle of the seven fourth-order Council Grove cycles suggests the possibility of higher-order cyclicity in the latter part of the middle Paleozoic icehouse. Large and small-scale patterns in the 3-D volume are especially useful in illustrating depositional model concepts discussed in Chapter 3, lithofacies distribution within and between cycles, and for the entire Wolfcamp (Figure 6.11). The 3-D view in the fence diagram format also illustrates the vertically heterogeneous, laterally continuous nature of the layered reservoir system.

One of the more striking aspects of the model from a reservoir perspective is the demonstration of lateral continuity in the lithofacies illustrated in Figures 6.12 through 6.19. County-scale “connected volumes” of the more significant reservoir lithofacies are sub-parallel to depositional strike and the field margin. Grain-supported packstone in the Crouse (Figure 6.12A, B1\_LM, Council Grove) is found primarily in the eastern half of the field while muddier lithofacies are dominant in the western, more sheltered shoreward portion of the shelf. These same relationships (grain-supported textures toward the shelf margin and muddier carbonate inboard) hold true for both the Council Grove (Figure 6.13 and 6.14) and Chase (Figure 6.15). However, the updip extent of rocks having grain-supported textures varies from cycle-to-cycle, most likely a function of changing hydrodynamics due to third-order cyclicity and overall global climatic shift from icehouse to greenhouse during the Lower Permian (Parrish and Peterson, 1988; Ross and Ross, 1988; Parrish, 1995; Rankey, 1997; Soreghan, 2002), discussed in detail in Chapter 3. In the Council Grove, the main pay lithofacies are packstone-grainstone (L7) and very fine crystalline dolomite (L6); however, the phylloid algal bafflestone lithofacies (L8) is important locally. Marine sandstone (L10) does not contribute to Council Grove production except for in the Grenola (C\_LM) in the very southwest corner of Texas County, Oklahoma (Figure 6.14), where the production is associated with a FWL that is different from that of the Hugoton-Panoma reservoir system (see Chapter 7).

Major contributing lithofacies (having good reservoir properties for storage and flow) are more variable in some Chase zones (Towanda, Krider, and Winfield) and their

contrasting spatial relationship is illustrated in the model (Figure 6.15). By far the most prolific reservoir lithofacies is medium-crystalline moldic dolomite (L9), which is restricted to the Chase. Other high-quality lithofacies are L7 and L10. L9, essentially dolomitized L7, is best developed in the middle to upper Chase (Towanda, Winfield, and Krider) while L7 is in the grain-supported category in the Wreford and Fort Riley. Marine sandstone contributes significantly to reservoir volume in the Towanda, Winfield, and Herington. Where two major reservoir lithofacies coexist in the Towanda, Winfield, and Krider, they tend to be best developed in different areas of the shelf rather than overlap (Figure 6.15).

Continental sandstone (eolian) is limited to the northwestern updip margin in the Council Grove (Figure 6.12B and 6.16), and shallow marine and tidal flat sandstone in the upper Chase is most abundant in the northwestern half of the field area (6.12C and Figure 6.17). Little continental sandstone occurs in the Chase while the occurrence of marine sandstone in the Council Grove is rare except as noted above. Noteworthy is that sandstone deposited in an offshore or deep-water environment is absent from the entire Wolfcamp and that sandstone is generally restricted to the updip (shoreward) portion of the shelf (see Chapter 3).

The core to model lithofacies workflow was sufficiently robust to characterize smaller important lithofacies bodies in the reservoir system (Figures 6.12-D, E, F, 6.18 and 6.19). For example, dolomitized grainstone and packstone of a relatively thick (30 ft, 10 m) carbonate ooid-bioclust-sand shoal system in the southern half of the field is known to be an important contributor to storage and flow capacity in the Krider (Sorenson, 2005, personal communication). Modeling of this important lithofacies shows the lateral continuity of a 4-mile-wide, 30-mile-long (6.5X50 km) “sweet spot” (porosity > 18%; Figures 6.12F and 6.18). By comparing screen captures of a 3-D view of this shoal in cross section and as a continuous volume (Figure 6.18) with 2-D map views of 3-D continuous volumes (Figure 6.15), a complete picture of the Krider reservoir system from fine to large scale is gained, illustrating the power of the cellular model. The main flow lithofacies (dolomitized ooid-bioclust) grainstone changes to packstone-grainstone of lower reservoir quality in a westerly direction, updip and towards the field margin as illustrated in cross-section (Figure 6.18) and map view (6.15). To the north, the shoal lithofacies changes to packstone-grainstone and wackestone of low reservoir quality. The connected volume approach, with the filter set in the high porosity range, captures the most prolific portion of an extremely large carbonate-sand system that covered much of Stevens County, Kansas, and north-central Texas County, Oklahoma.

Another interesting set of geobodies that are effectively characterized in the cellular geomodel is a phylloid algal-mound system in the Cottonwood Limestone Member (B5\_LM) shown in Figure 6.19. Map views of 3-D connected volumes of three lithofacies, packstone-grainstone, very fine-crystalline dolomite, and phylloid algal bafflestone, suggest a patchwork of lithofacies. Closer examination in 3-D cross section and blocked lithofacies at the node wells better illustrates the overlapping nature of the three discrete lithofacies and their interrelationships. The relatively thick mound facies (20 ft, 6 m in the Churchman Bible, a cored well) tends to occur in the lower half of the

Cottonwood and is interpreted as being deposited in moderate water depths. Dolomitized mudstone and wackestone (L6) occupy much of the inter-mound space and packstone-grainstone (L7) caps the shoaling-upward cycle. Algal mounds are most common in the Cottonwood (B5\_LM) and Crouse (B1\_LM) and are effective reservoirs where algal grains are dissolved to form large connected moldic porosity in a position above the FWL. Unfortunately, most of the mounds in the Cottonwood are below the FWL and are non-productive.

### **Property Distribution in the Model**

Distributions of lithofacies-dependent properties (porosity, permeability and water saturation) reflect the lithofacies distribution (Figure 6.20), as one would expect. The best porosity and permeability coincide with the main reservoir lithofacies (Figure 6.13). Laterally extensive low permeability intervals separate the relatively high permeability pay zones of the layered reservoir system. Water saturations are high in the confining intervals and the “gas-water” contact crosses stratigraphic boundaries at the east downdip margin as the pay intervals dip below the surface and on the west where the free water level is thought to rise more quickly than the rate of dip.

## **6.5 POROSITY MODEL**

*Martin K. Dubois and Geoffery C. Bohling*

The principal tasks involved in development of the Porosity Model included compilation and quality analysis of the industry and KGS LAS well-log files at node wells as described in Chapter 4 and in section 6.2, above. Corrections to standard porosity log curves are discussed in Chapter 4 and below. The development of the variograms used within Petrel<sup>TM</sup> for populating grid cells between wells and the modeling process is also discussed.

### **Porosity correction (PhiCorr)**

Because porosity correction algorithms (Chapter 4, section 4.3) are lithofacies dependent it is only after lithofacies have been generated for all node wells that log porosity can be adjusted. After lithofacies have been predicted and lithofacies curves have been assembled in another application (by merging or otherwise), we applied the lithofacies-dependent algorithms discussed in Chapter 4, section 4.3, to correct for the influence of mineralogical variations, gas effect, and washouts on log porosities, employing the following steps:

1. Generate LAS format files containing Nphi (decimal), Dphi (decimal, 2.71 matrix), N-Dphi (decimal, average), and lithofacies coded from 1-11, one well per file and placed in a single folder.

2. Correct porosity for mineralogy and washout effects using an automated porosity correction tool developed for the project. Output is corrected porosity in a LAS file format.
3. Import LAS files with corrected porosity into another application and check for quality.

## **Modeling Porosity**

As in the case for lithofacies modeling, voxel-based methods were chosen over object-based methods due to the relatively dense well control and geometry of the lithofacies bodies being modeled (thin and laterally extensive). Corrected porosity curves were read into Petrel<sup>TM</sup> and upscaled from 1/2-ft (0.15 m) to layer scale (2-4 ft) using arithmetic averaging, biased by upscaled lithofacies at the node wells. Porosity values over the entire model (between node wells) were generated using sequential Gaussian simulation (Deutsch and Journel, 1998) as implemented in Petrel<sup>TM</sup>, utilizing porosity transforms generated with the application's data analysis tool and conditioned by lithofacies. The stochastic simulation procedures require the specification of a variogram model for each lithofacies, describing the spatial correlation behavior of the property being simulated.

## **Porosity Variograms**

The process for computing and fitting the porosity variograms was essentially identical to that for the lithofacies variograms, except for the scaling step. Continuous variables like porosity are typically passed through a normal score transform, essentially replacing the original data with perfectly normally distributed data, prior to variogram computation and simulation, and this step is included in the variogram computation scripts. Again, this transformation is applied on a layer-by-layer basis for the horizontal variograms, to try to reduce the influence of zonal anisotropy. Overall, the behavior of the porosity variograms is similar to that of the lithofacies variograms, except that the porosity variograms are noisier overall. Figures 6.21 and 6.22 show the vertical and horizontal variograms for porosity in lithofacies 5 over all six subintervals, along with the fitted models. The most noticeable difference in behavior relative to the lithofacies variograms is that the vertical porosity variograms are considerably noisier. This behavior is typical for all lithofacies.

## **6.6 PETROPHYSICAL MODEL**

*Alan P. Byrnes and Martin K. Dubois*

### **Model Permeability and Saturations**

In addition to populating gridcells with lithofacies and porosity, as discussed above, the workflow process involves populating the gridcells with permeabilities ( $k_{xy}$  and  $k_z$ ) and

fluid saturations. Modeling petrophysical properties for each cell of the geomodel requires utilization of 1) the petrophysical algorithms, discussed in Chapter 4 section 4.2, 2) the lithofacies model discussed above, where lithofacies is assigned to each of the 108-million gridcells, 3) the porosity ( $\phi$ ) model discussed above, and 4) for water saturations and relative permeability, the capillary-pressure models discussed in Chapter 4, section 4.2, and the free-water level model discussed in Chapter 7 section 7.2.

As noted, the porosity and lithofacies models were upscaled from the initial half-ft thick scale to the scale of model layers (roughly 2-ft thick in marine intervals and 4-ft thick in non-marine intervals). Lithofacies were upscaled vertically by “majority vote” where the lithofacies for each model cell intersecting a well was taken to be the most frequently occurring lithofacies in that layer in the well. Porosity was upscaled vertically using facies-biased arithmetic averaging. For the lithofacies distributions for each layer, this averaging method calculated average porosity values that were negligibly different from an arithmetic average. Using these upscaled values at the node well gridcells, the complete 108-million cell geomodel was populated with lithofacies and porosity values utilizing the variograms and spatial interpolation algorithms input into Petrel™. In addition, the free-water level elevation was assigned for each XY location utilizing the input free-water level database. Details on upscaling lithofacies and porosity are presented in appendix *Geomod4\_build*.

Using the porosity and lithofacies data in each gridcell, *in situ*- Klinkenberg gas permeability ( $k_{ik}$ ) was calculated for each gridcell using the equations presented in Table 4.2.6 with input of the lithofacies and porosity of the gridcell. Vertical permeability ( $k_{vert}$ ) was calculated for each cell by multiplying the calculated horizontal permeability,  $k_{ik}$ , by the average  $k_{vert}/k_{havg}$  ratio for each lithofacies, as presented in Chapter 4, section 4.2. Water saturation ( $S_w$ ) and gas saturation ( $S_g = 1 - S_w$ ) were calculated for each gridcell utilizing 1) the lithofacies-porosity-specific capillary-pressure equations summarized in Table 4.2.8, 2) the lithofacies of the gridcell, 3) the porosity of the gridcell, 4) the gridcell elevation, and 5) the free-water level elevation at the XY location of the gridcell. Finally, original gas in place (OGIP) for each gridcell was calculated:

$$OGIP = V_{gridcell} \phi S_g E_g$$

Where  $V_{gridcell}$  is the volume of the gridcell and  $E_g$  is the gas expansion factor appropriate for the input reservoir gas composition at the input initial reservoir pressure and temperature, defined in the fluid properties database, and discussed in Chapter 10.

Gas- and water-relative permeability properties were not calculated for each gridcell in the static model because relative permeability curves presented in Chapter 4, section 4.2, were input into the dynamic model, as discussed in Chapter 9. Though it was not performed, relative permeabilities could have been calculated for each gridcell using the relative permeability equations discussed in Chapter 4, section 4.2, and the calculated water saturations ( $S_w$ ) discussed above.

### **Influence of Upscaling on Properties**

The process of geomodel construction involves the upscaling of lithofacies and porosity from the half-ft scale to the 2-ft to 4-ft thick layer scale. For the geomodels constructed, permeability was calculated from the upscaled-layer porosities and not the half-ft scale porosities. This introduces the potential for model-calculated permeabilities to have different values from layer permeabilities that might be calculated by upscaling permeability values calculated at the half-ft (i.e., bed) scale. The potential difference between these two methods of calculating permeability is dependent on the range in porosity that exists within the layer, the half-ft scale lithofacies present in the layer, the lithofacies assigned to the total layer, and the  $k$ - $\phi$  relations of the lithofacies. To examine how much difference could exist between these permeability-calculation methods, the two methods were compared for the Flower A-1 well, which is considered representative of the range of properties often encountered. Model layer permeability compared are those from the 70 mi<sup>2</sup>, 209-layer static model constructed specifically for the Flower simulation model (Chapter 9), built in the same manner and nearly identical property transforms as the full-field geomodel. Model zone permeability was extracted from the Flower 25-zone simulation model that was upscaled from the static model.

In the Flower A-1, the Chase and Council Grove Groups range over a depth of 2473 ft to 2972 ft, representing 998 half-ft intervals. These half-ft intervals were upscaled to 209 layers as shown in Figure 6.23. For these layers an average porosity was calculated arithmetically and the principal lithofacies assigned to each layer. Permeability ( $k_{\text{avg-layer}}$ ) was calculated for each layer using the layer porosity and layer lithofacies and the  $k$ - $\phi$  equation presented in Table 4.2.6. Figure 6.24 shows a comparison between the layer permeabilities ( $k_{\text{avg-layer}}$ ) and permeabilities that were calculated by arithmetically averaging the permeabilities of the half-ft beds contained within the layer ( $k_{\text{avg-bed}}$ ). Figure 6.25 shows a histogram of the ratio of the layer-permeability to the bed-upscaled permeability ( $k_{\text{avg-layer}}/k_{\text{avg-bed}}$ ).

As discussed in Chapter 8, section 8.1, in a parallel-flow architecture, permeabilities calculated for a single  $k$ - $\phi$  transform from an average porosity are always less than the arithmetically averaged permeability calculated from the individual-porosity intervals from which the average porosity was comprised. The cumulative frequency distribution in Figure 6.25 shows that for approximately 10% of the layers, the layer-upscaling method under-predicts permeability by greater than a factor of 5. For approximately 10% of the layers, this method under-predicts permeability by a factor of 2 to 5. Only for ~5% of the layers is the layer-permeability greater than 2 times the bed-upscaled permeability, and in only 0.5% is the layer-permeability greater than 5 times the bed-upscaled permeability. For a vertical set of rocks of identical lithofacies, the  $k_{\text{avg-layer}}/k_{\text{avg-bed}}$  ratio never exceeds a value of 1. The reason this ratio exceeds 1 in a small fraction of the population is that for these layers the lithofacies assigned to the layer exhibits a higher permeability-porosity trend than some fraction of the bed lithofacies. Layers for which the  $k_{\text{avg-layer}}/k_{\text{avg-bed}}$  ratio is less than 0.5 generally exhibit a large difference in permeability due to the presence of a thin, significantly higher-permeability bed, relative to the other beds in the layer. Figure 6.24 illustrates that differences between these permeability-calculation methods can occur for layers of widely varying upscaled

permeability, although differences of greater than a factor of 2 occur less frequently for layers with permeability > 1 md (10%) compared to layers with permeability < 1 md (20%). Eliminating the low skewed samples, the methods can be characterized as agreeing with a standard deviation of 40% (i.e., 75% of the permeabilities agree within the  $k_{\text{avg-layer}}/k_{\text{avg-half-ft}}$  range of 0.6-1.4). This difference between these permeability-calculation methods is not significant and falls within the standard errors of prediction of permeability from porosity and lithofacies, which exhibit an average error of 5.1X (Chapter 4, section 4.2).

## Upscaling the Static Model to the Dynamic Model

The 108-million cell static geomodel provided a detailed and precise model for defining reservoir properties throughout the Hugoton area. Challenges posed by the large model size were handled by subdividing the model into six layers, as discussed above. However, for dynamic reservoir simulation modeling that was utilized to investigate regional flow or communication between layers, the large number of gridcells in the geomodel precluded the direct use of this model in dynamic reservoir simulation. To reduce the number of gridcells in the geomodel to a size that could be utilized conveniently by the reservoir simulation software, static geomodel properties were upscaled. In this process, the properties of the 2-ft to 4-ft thick layers were upscaled to 10-ft to 50-ft thick zones where each zone represents the half-cycle of a stratigraphic member (i.e., a stratigraphic member is composed of two zones, a marine half-cycle zone and nonmarine half-cycle zone). The thicknesses of the zones were determined by the stratigraphic tops and gridcell thicknesses at the given XY location. Porosity and water saturation were upscaled using volume-weighted arithmetic averaging. Permeability was upscaled using the PSK-solver tensor algorithm in Petrel™. Details on upscaling the static model to the dynamic reservoir simulation model are presented in the digital appendix *Geomod4\_build* and properties are discussed in Chapter 9.

As with the upscaling of layers discussed above, the upscaling of layers to zones introduced the potential for differences between permeabilities calculated from layers and those calculated using the PSK-solver tensor analysis. Figure 6.26 shows a crossplot for 25 zones upscaled from the 209 layers of average-zone permeabilities calculated using tensor- and volume-weighted arithmetically averaged layer permeabilities (where the zone permeability represented the volume-weighted arithmetic average of all the layers within the zone) versus bed arithmetically average permeability for the zone (i.e., where the zone permeability represented the arithmetic average of all half-foot thick beds in the zone). Layer- and tensor-calculated zone permeabilities average  $80 \pm 30\%$  (error is 1 standard deviation) of the bed-permeabilities. Layer-permeabilities average 97% of tensor-calculated permeabilities indicating little difference between these calculation methods. This close correspondence is primarily because the tensor solution for permeability has little effect for vertically stacked single cells where parallel flow dominates. If the system being upscaled involved a greater number of cells horizontally, it would be anticipated that the tensor-calculated zone permeabilities would exhibit greater permeability as a function of the presence of thin high-permeability layers. In

Figure 6.26 there are four zones for which the bed-upscaled zone permeability is significantly greater than the layer- and tensor-calculated zone permeabilities. Without exception each of these zones contains one or two layers where the layer permeabilities ( $k_{\text{avg-layer}}$ ) were significantly less than the bed-upscaled permeability ( $k_{\text{avg-bed}}$ ) due to the presence of thin, high-permeability beds. Some zones contain one or two layers that exhibit exceptionally low permeability but these do not significantly affect the zone average permeabilities.

## References

- Bohling, G. C., and J. H. Doveton, 2000, Kipling.xla: An Excel Add-in for Nonparametric Regression and Classification: Kansas Geological Survey, <http://www.kgs.ku.edu/software/Kipling/Kipling1.html>. (Accessed June 15, 2006)
- Deutsch, C. V., 2002, Geostatistical Reservoir Modeling: Oxford University Press, New York, 376 p.
- Deutsch, C. V., and A. G. Journel, 1998, GSLIB: Geostatistical Software Library and User's Guide, Second Edition: Oxford University Press, New York, 369 p.
- Dubois, M. K., A. P. Byrnes, G.C. Bohling, S. C. Seals, and J. H. Doveton, 2003, Statistically-based lithofacies predictions for 3-D reservoir modeling: examples from the Panoma (Council Grove) field, Hugoton embayment, southwest Kansas (abs): Proceedings American Association of Petroleum Geologists 2003 Annual Convention, Salt Lake City, Utah, v.12, p. A44, and Kansas Geological Survey Open-file Report 2003-30, 3 panels, <http://www.kgs.ku.edu/PRS/publication/2003/ofr2003-30/index.html> (accessed August 23, 2006).
- Dubois, M.K., A.P. Byrnes, G.C. Bohling, and J.H. Doveton, 2006, Multiscale geologic and petrophysical modeling of the giant Hugoton gas field (Permian), Kansas and Oklahoma: in P. M. Harris and L. J. Weber, eds., Giant Reservoirs of the World: From Rocks to Reservoir Characterization and Modeling: American Association of Petroleum Geologists, Memoir 88, p. 307-353.
- Fetkovitch, M. J., D. J. Ebbs Jr., and J. J. Voelker, 1994, Multiwell, multilayer model to evaluate infill-drilling potential in the Oklahoma Hugoton field: Society of Petroleum Engineers, 65th Annual Technical Conference and Exhibition, New Orleans, Paper SPE 20778, p. 162-168.
- Garlough, J. L., and G. L. Taylor, 1941, Hugoton gas field, Grant, Haskell, Morton, Stevens, and Seward counties, Kansas, and Texas County, Oklahoma: in A. I. Levorsen,, ed., Stratigraphic Type Oil Fields: American Association of Petroleum Geologists, Tulsa, p. 78-104.

Hastie, T., R. Tibshirani, and J. Friedman, 2001, *The Elements of Statistical Learning: Data Mining, Inference, and Prediction*: Springer-Verlag, New York, 533 p.

Heyer, J. F., 1999, Reservoir characterization of the Council Grove Group, Texas County, Oklahoma: *in* D. F. Merriam, ed., *Geosciences for the 21<sup>st</sup> Century: Transactions of the American Association of Petroleum Geologists Midcontinent Section Meeting*, Wichita, KS, p. 71-82.

Hubbert, M. K., 1953, Entrapment of petroleum under hydrodynamic conditions: *American Association of Petroleum Geologists, Bulletin*, v. 37, p. 1954-2026.

Oberst, R. J., P. P. Bansal and M. F. Cohen, 1994, 3-D reservoir simulation results of a 25-square mile study area in Kansas Hugoton gas field: *Society of Petroleum Engineers Mid-Continent Gas Symposium*, Amarillo, TX, Paper SPE 27931, p. 137-147.

Olson, T. M., J. A. Babcock, K. V. K. Prasad, S. D. Boughton, P. D. Wagner, M. K. Franklin, and K. A. Thompson, 1997, Reservoir characterization of the giant Hugoton Gas Field, Kansas: *American Association of Petroleum Geologists, Bulletin*, v. 81, p. 1785-1803.

Parham, K. D., and J. A. Campbell, 1993, PM-8. Wolfcampian shallow shelf carbonate-Hugoton Embayment, Kansas and Oklahoma: *in* D. G. Bebout, ed., *Atlas of Major Midcontinent Gas Reservoirs*: Gas Research Institute, p. 9-12.

Parrish, J. T., 1995, Geologic evidence of Permian climate: *in* P. A. Scholle, T. M. Peryt, and D. S. Ulmer-Scholle, ed., *The Permian of northern Pangea, Volume I; Paleogeography, Paleoclimate, Stratigraphy*, Berlin, Germany, Springer-Verlag, p. 53-61.

Parrish, J. T. and E. Peterson, 1988, Wind Directions Predicted from Global Circulation Models and Wind Directions Determined from Eolian Sandstones of the Western United States - A Comparison: *Sedimentary Geology*, v. 56, p. 261-282.

Pebesma, E. J., 2004. Multivariable geostatistics in S: the gstat package: *Computers & Geosciences*, v. 30, p. 683-691.

Pippin, L., 1970, Panhandle-Hugoton field, Texas-Oklahoma-Kansas-The first fifty years; *in* M. T. Halbouty (ed.), *Geology of Giant Petroleum Fields*: American Association of Petroleum Geologists, Memoir 14, Tulsa, p. 204-222.

R Development Core Team, 2005, *R: A language and environment for statistical computing*; R Foundation for Statistical Computing, Vienna, Austria, <http://www.R-project.org>. (accessed September 23, 2006)

Rankey, E. C., 1997, Relations between relative changes in sea level and climate shifts; Pennsylvanian-Permian mixed carbonate-siliciclastic strata, western United States, *Geological Society of America, Bulletin*, vol. 109, no. 9, p. 1089-1100.

Ross C. A. and J. R. P. Ross, 1988, Late Paleozoic transgressive-regressive deposition.: Society of Economic Paleontologists and Mineralogists Special Publication 42, p. 227-247.

Seimers, W. T., and W. M. Ahr, 1990, Reservoir facies, pore characteristics, and flow units: Lower Permian Chase Group, Guymon-Hugoton Field, Oklahoma: Society of Petroleum Engineers Proceedings, 65th Annual Technical Conference and Exhibition, New Orleans, LA, September 23-26, 1990, Paper SPE 20757, p. 417-428.

Soreghan, G. S., R. D. Elmore, and M. T. Lewchuk, 2002a, Sedimentologic-magnetic record of western Pangean climate in upper Paleozoic loessites (lower Cutler beds, Utah): Geological Society of America Bulletin, v. 114, no. 8, p.1019-1035.

Sorenson, R. P., 2005, A dynamic model for the Permian Panhandle and Hugoton fields, western Anadarko basin: American Association of Petroleum Geologists, Bulletin, v. 89, no. 7, p. 921-938.

Venables, W. N., and B. D. Ripley, 2002, Modern Applied Statistics with S, Fourth Edition: Springer, New York, 512 p.

Chase	Cgrv
HRNGTN	A1_SH
KRIDER	A1_LM
ODELL	B1_SH
WINF	B1_LM
GAGE	B2_SH
TWND	B2_LM
B/TWND	B3_SH
FTRLY	B3_LM
B/FTRLY	B4_SH
WREFORD	B4_LM
	B5_SH
	B5_LM
	C_SH
	C_LM
	D_SH

**Table 6.1** Tops set for 25 formation/member level (1/2-cycle) intervals, or zones in the cellular geo-model. Seven of the tops were used for the structural framework: Herington (HRNGTN), Winfield (WINF), Fort Riley (FTRLY, Speiser (A1\_SH), Middleburg (B2\_LM), Morrill (B4\_LM), and Base of Grenola (D\_SH).

**4 Header files:**

Framework only	7250	
LAS_Both Chase-Cgrv	954	
LAS Cgrv only	294	
LAS Chse only	352	total 8850

**3 Tops files:**

Framework (7tops)	8556 = 7250 + 1306 (Chase LAS 954 + 352)
Chase (11 tops)	1306 with LAS
Council Grove (15 tops)	1248 with LAS

**LAS files:**

GR, PhiCorr and Lithofacies

**7 Framework Grids:**

Herington, Winfield, Ft Riley, A1\_SH, B2\_LM, B4\_LM, and D\_SH

**Free Water Level Grid**

**Table 6.2.** Input files required for building cellular geomodel. Abbreviations include: LAS – Log ASCII Standard format; Cgrv – Council Grove.

# Chase Group – Lithofacies variograms

- General Rules:**
1. Horizontal major axes are average for either the Chase or Wolfcamp (Chase & Council Grove)
  2. For lithofacies 3-10, minor axis is 5/6th of major (as in Geomod3). Seemed to work fine in Geomod3.
  3. Azimuth is 11 degrees, same as in Geomod3. This is approximate regional strike.
  4. Vertical ranges are average for either the Chase or Wolfcamp (Chase & Council Grove).
  5. Used shorter vertical ranges for facies that are out of place for the zone
  6. Nugget = 0 and Sill = 1

Chase Group						Rationale
Facies	Major (k-ft)	Minor (k-ft)	Az	Vertical (ft)	Horizontal	Vertical
0	30	30		17	Poor*	Chase
1	25	25		17	Poor*	Chase
2	25	25		17	Poor*	Chase
3	24	20	11	11	Wolfcamp	Chase
4	18	15	11	7	Wolfcamp	Chase
5	18	15	11	7	Wolfcamp	Chase
6	30	25	11	16	Wolfcamp	Wolfcamp
7	27	23	11	16	Chase	Chase
8	NA	NA	NA	NA	None in Chase	None in Chase
9	27	23	11	16	Poor, same as F7*	Poor, same as F7*
10	25	21	11	21	Chase	Chase

Major axis is average for Chase or Wolfcamp (Chase & Council Grove)  
 Minor axis is 5/6th of major (as in Geomod3)  
 Azimuth = 11 degrees, as in Geomod 3  
 Rationale:  
 Chase Used average for Wlfcmp (Chase & Council Grove)  
 Wolfcam Used average for Chase  
 Poor\* One HZ variogram in Chase F0-F2 = 29902.  
 \*F9 variogram parameters modified later for more deterministic outcome

# Chase Group – Porosity variograms

CHASE						Rationale
Facies	Major (k-ft)	Minor (k-ft)	Az	Vertical (ft)	HZ	VERT
0	42	42		25	Poor*	Cgrv, NA in Chase
1	35	35		15	Poor*	Wolfcamp
2	35	35		9	Poor*	Wolfcamp
3	32	27	11	16	Wlfcmp	Wolfcamp
4	32	27	11	16	NA, used F3	NA, used F4
5	36	30	11	21	Cgrv, NA in chase	Wolfcamp
6	27	23	11	17	Cgrv, NA in chase	Wolfcamp
7	34	28	11	14	Cgrv, NA in chase	Wolfcamp
8	NA	NA	NA	NA	None in Chase	None in Chase
9	39	33	11	20	Poor, same as F7	Chase
10	37	31	11	20	Chase	Chase

- General Rules:**
1. Horizontal major axes are average for either the Chase or Wolfcamp (Chase & Council Grove), except F0-2
  2. Range for F0-2 are proportionately larger than for facies
  3. For lithofacies 3-10, minor axis is 5/6th of major (as in Geomod3). Seemed to work fine in Geomod3.
  4. Azimuth is 11 degrees, same as in Geomod3. This is approximate regional strike.
  5. Vertical ranges are average for either the Chase or Wolfcamp (Chase & Council Grove).
  6. Used shorter vertical ranges for facies that are out of place for the zone (5 feet)
  7. Nugget = 0 and Sill = 1

**Table 6.3.** Variograms ranges used in modeling lithofacies and porosity in the Chase Group, less the Wreford. Top is a summary table showing the mean value for horizontal and vertical variogram ranges by lithofacies, the stratigraphic interval from which the mean was calculated, and rules employed to develop the table. A similar table for porosity variogram ranges is shown at the bottom.

## Council Grove Group – Lithofacies variograms

- General Rules:**
- Where available, horizontal major axes are average for Council Grove.
  - For lithofacies 3-10, minor axis is 5/6th of major (as in Geomod3). Seemed to work fine in Geomod3.
  - Azimuth is 11 degrees, same as in Geomod3. This is approximate regional strike.
  - Where available vertical ranges are average Council Grove.
  - Used shorter vertical ranges for facies that are out of place for the zone
  - Nugget = 0 and Sill = 1

Council Grove				Rationale		
Facies	Major (k-ft)	Minor (k-ft)	Az	Vertical (ft)	Horizontal	Vertical
0	40	40		10	Poor est	Poor est
1	25	25		10	Cgrv	Cgrv
2	25	25		8	Cgrv	Cgrv
3	30	25	11	11	Cgrv	Cgrv
4	18	15	11	7	Cgrv	Cgrv
5	18	15	11	7	Cgrv	Cgrv
6	30	25	11	10	Cgrv	Cgrv
7	18	15	11	5	Cgrv	Cgrv
8	18	15	11	5	NA, same as F7	NA, same as F7
9	NA	NA	NA	NA	None in Cgrv	None in Cgrv
10	25	21	11	21	Chase	Chase

F0 poor in analysis, estimated in modeling  
 F3 1 value = 43k, used 30k  
 F4 not enough data  
 F6 avg = 33k, used 30k  
 F8, 10 not enough data  
 F9 Not present

## Wreford and Council Grove Group – Porosity variograms

### Wreford and Council Grove

Wreford and Council Grove					Rationale	
Facies	Major (k-ft)	Minor (k-ft)	Az	Vertical (ft)	HZ	VERT
0	42	42		15	Poor*	Cgrv, NA in chase
1	35	35		12	Poor*	Cgrv
2	35	35		9	Poor*	Wolfcamp
3	32	27	11	16	Wolfcamp	Wolfcamp
4	32	27	11	16	NA, used F3	NA, used F4
5	36	30	11	17	Cgrv, NA in chase	Cgrv
6	27	23	11	14	Cgrv, NA in chase	Cgrv
7	34	28	11	14	Cgrv, NA in chase	Cgrv
8	34	28	11	14	NA, used F7	NA, used F7
9	NA	NA	NA	NA	NA	Not in Cgrv
10	37	31	11	15	Chase	Reduced

**General Rules:**

- Horizontal major axes are average for either the Chase or Wolfcamp (Chase & Council Grove), except F0-2
- Range for F0-2 are proportionately larger than for facies
- For lithofacies 3-10, minor axis is 5/6th of major (as in Geomod3). Seemed to work fine in Geomod3.
- Azimuth is 11 degrees, same as in Geomod3. This is approximate regional strike.
- Vertical ranges are average for either the Chase or Wolfcamp (Chase & Council Grove).
- Used shorter vertical ranges for facies that are out of place for the zone (5 feet)
- Nugget = 0 and Sill = 1

**Table 6.4.** Variograms ranges used in modeling lithofacies and porosity in the Wreford and Council Grove Group. Top is a summary table showing the mean value for horizontal and vertical variogram ranges by lithofacies, the stratigraphic interval from which the mean was calculated, and rules employed to develop the table. A similar table for porosity variogram ranges is shown at the bottom.

	Height	0.5 feet	0.5 feet	Variable*	Variable*
	Source	Actual	NNet Predicted	Upscaled	Modeled (SIS)
Code	Lithofacies	Training	Node Wells	Node Wells	All cells
0	Cont SS	3.8%	2.4%	1.4%	1.8%
1	Cont Crs Slt	21.0%	18.6%	15.0%	14.6%
2	Cont Fn Slt	11.2%	8.9%	7.7%	7.8%
3	Mar Slt	7.6%	9.6%	9.7%	9.9%
4	Mdst	6.1%	1.6%	1.3%	1.6%
5	Wkst	13.4%	19.7%	22.2%	24.5%
6	Vf-fxln Dol	3.4%	3.5%	3.5%	3.6%
7	Pkst-Grnst	18.2%	22.1%	24.7%	23.9%
8	PA Baff	0.8%	0.6%	0.7%	0.7%
9	F-mxln Dol	7.3%	6.6%	6.9%	4.7%
10	MM SS	7.0%	6.4%	6.9%	7.0%
<b>Count (N)</b>		13,512	1,383,653	211,720	108,064,831

\* Model layer h. Average of mean h = 3.3 feet. Range of mean h = 1.9 to 5.2 feet. Lithofacies 0-2 tend to be in thicker layers.

**Table 6.5.** Relative distribution of 11 lithofacies in core, node wells, and cellular model. Core-defined lithofacies for 28 wells were used in neural network “Training” for lithofacies prediction in 1600 “Node Wells.” Half-ft (0.15 m) lithofacies in node wells were upscaled to model layer thickness (Variable Upscaled). Sequential indicator simulation (SIS) was utilized to populate the cellular model (All Cells) between the node wells.

# Model Development Workflow

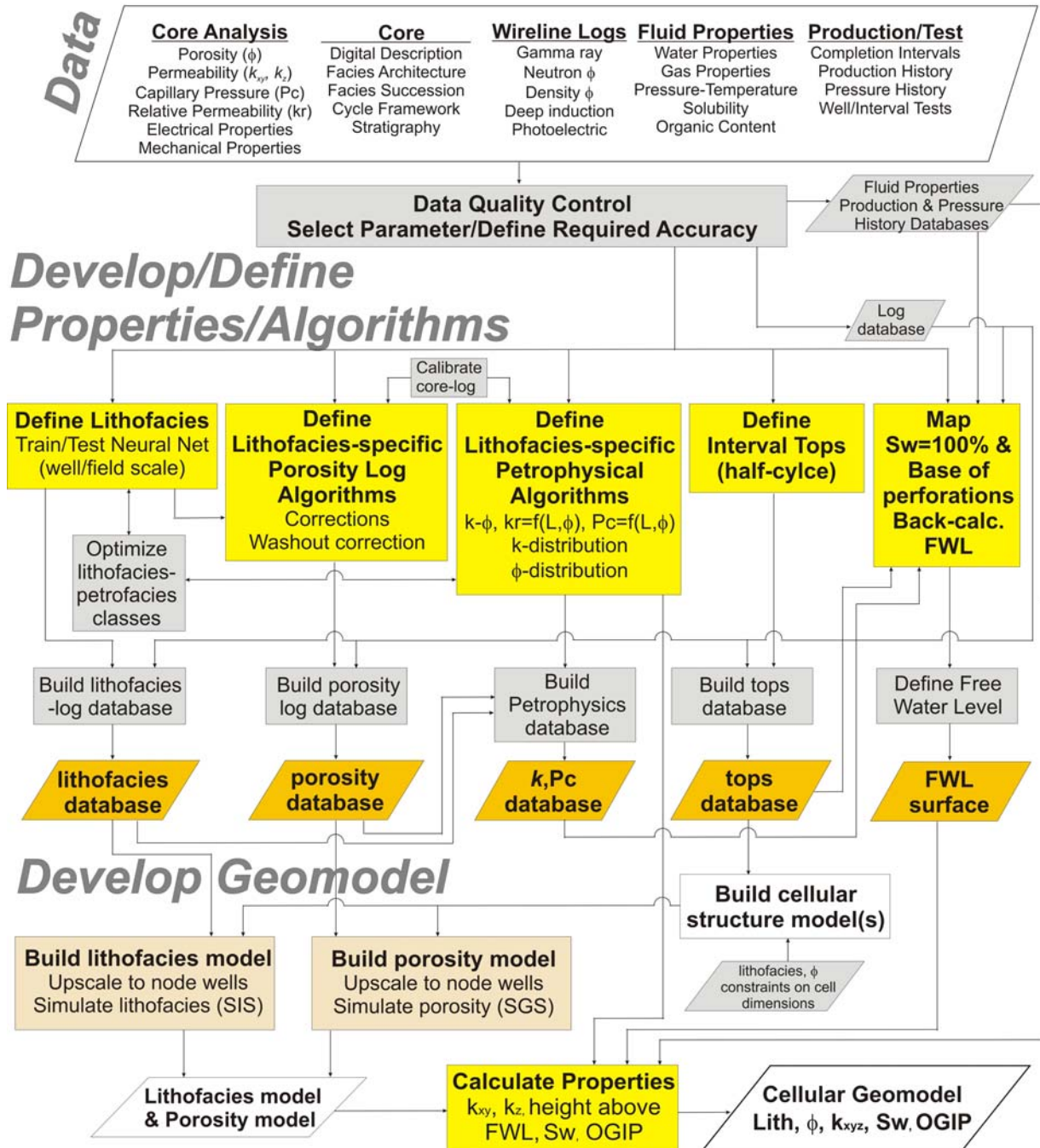


**Figure 6.1.** Workflow for field-scale Hugoton model. Workflow can be divided into three broad tasks: 1) gather and qualify data; 2) process data to provide basic geomodel input files (Develop/ Define/ Properties/ Algorithms); and 3) build the geomodel. The figure suggests the process is linear, while in reality, there are more feedback loops, multiple iterations at sub-task level, and testing and validation at smaller scales.

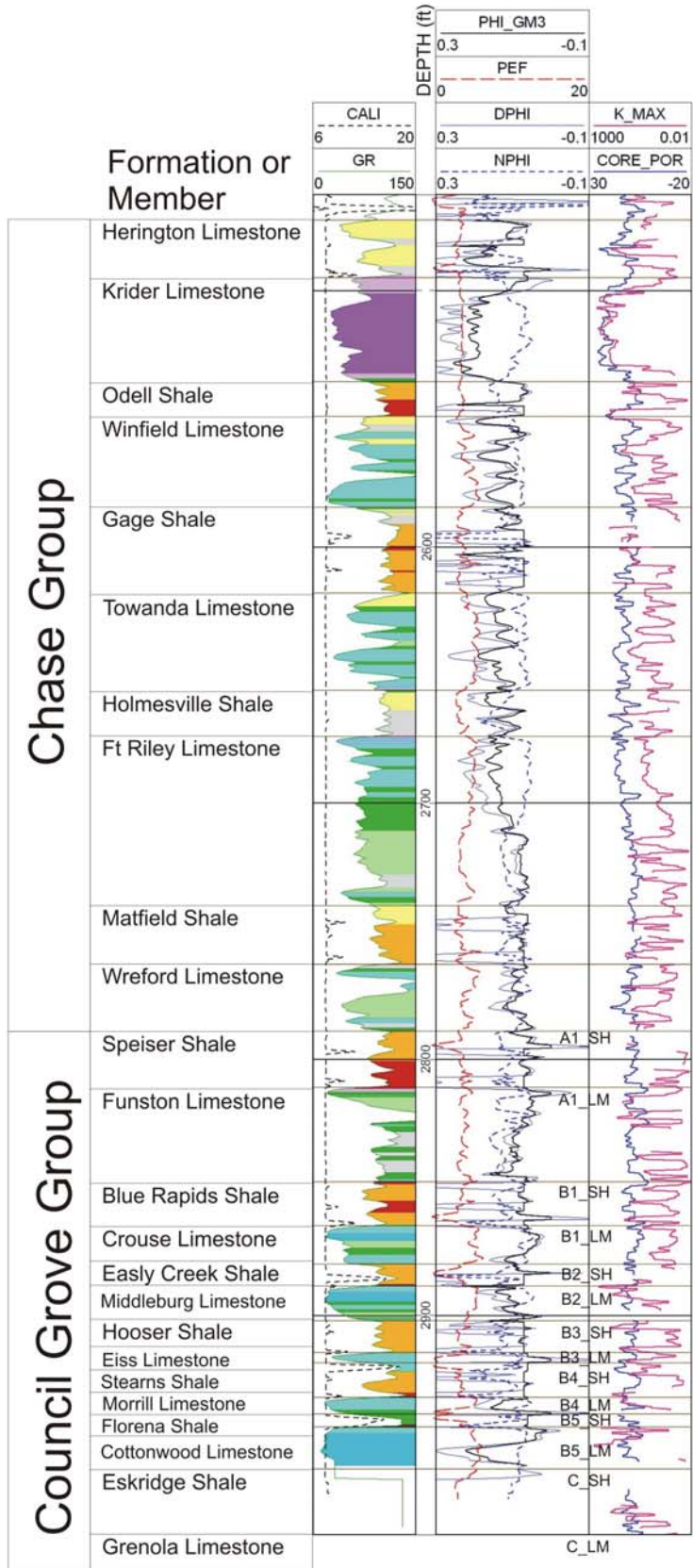


**Figure 6.2.** Formation- and member-level stratigraphy correlated to wireline well log in the Flower A-1 well, Stevens County, Kansas. Commonly used formation/member letter-number combinations are shown for the Council Grove. Twelve of the 13 marine-continental (carbonate-siliciclastic) sedimentary cycles that are gas productive are shown (Grenola Limestone, C\_LM is not logged). Stratigraphic names that include "Limestone" are marine half-cycles, that when combined with an adjacent continental half-cycle intervals with stratigraphic names that include "Shale," form a complete cycle. Color-coded lithofacies are derived from core. Three were deposited in a continental setting, L0- sandstone, L1- coarse siltstone, and L2- shaly siltstone, and eight in a marine environment, L3- siltstone, L4- carbonate mudstone, L5- wackestone, L6- very fine-crystalline dolomite, L7- packstone-grainstone, L8- phylloid algal bafflestone, L9- fine-medium crystalline moldic dolomite, and L10- sandstone. Wireline log abbreviations are caliper (CALI), gamma ray (GR), corrected porosity (PHI\_GM3), photoelectric effect (PEF), density porosity (DPHI), neutron porosity (NPHI), core permeability (K\_MAX, and core porosity (CORE\_POR). Logged interval is 520 ft (160 m).

- 10
- 9
- 8
- 7
- 6
- 5
- 4
- 3
- 2
- 1
- 0

**Lithofacies Code**

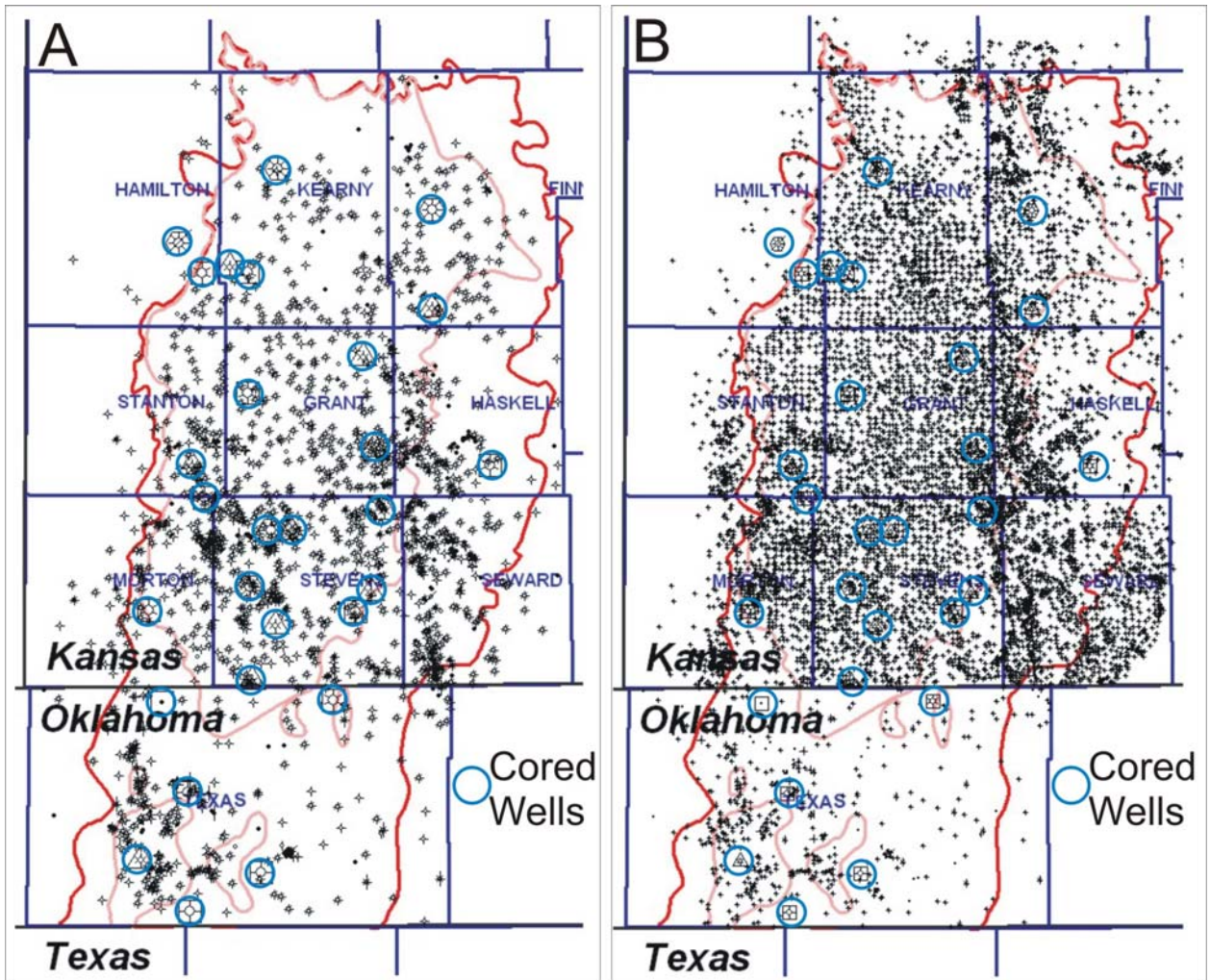


**Figure 6.3. (A)** Map illustrating location of 1600 node wells used for the static model construction. Fourteen of the wells have core-defined lithofacies (circled) and the balance have lithofacies predicted by neural networks. The 1600 are a mix of Council Grove (1256) and Chase (1314) wells with lithofacies defined by neural net (1209 of the 1600 have both Council Grove and Chase lithofacies). Only wells with lithofacies defined at least to the top of the Fort Riley (Chase) or the Florena Shale, B5\_SH (Council Grove) were considered. **(B)** Map showing 8850 wells with formation-member level tops used for building the structural and stratigraphic framework for the Hugoton geologic model.

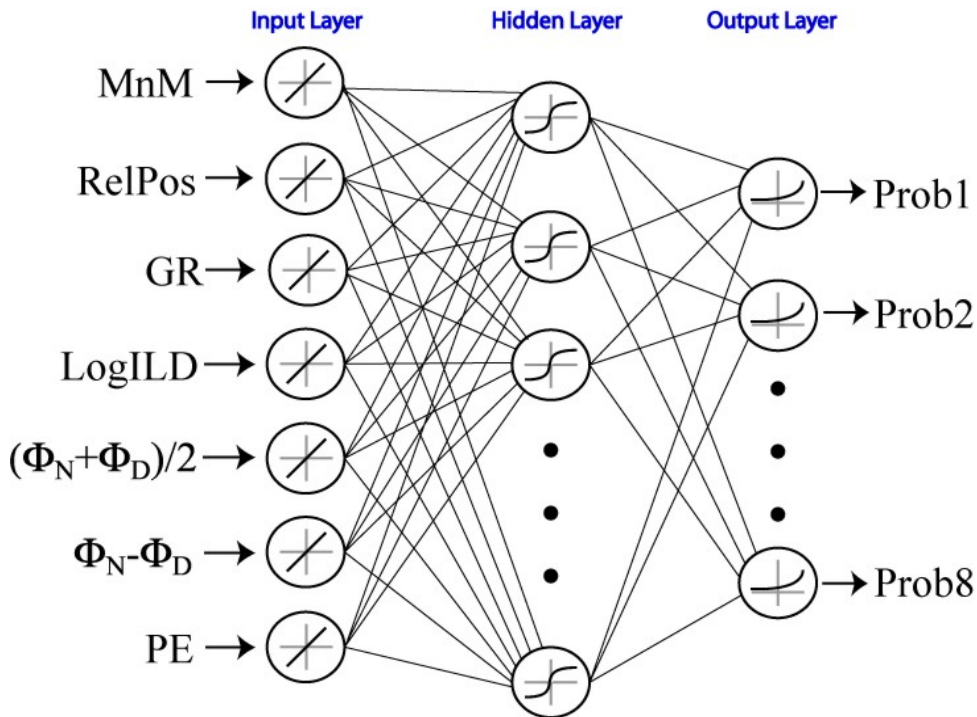


**Figure 6.4.** Schematic representation of single hidden-layer neural network used to predict lithofacies from wireline logs and geologic constraining variables. Inputs two geologic constraining variables (MnM – depositional environment indicator; RelPos – relative position in stratigraphic interval); and array of nuclear and electrical wireline log curves: gamma ray, (GR); logarithm of deep induction log (LogILD); average of neutron and density porosity  $(\Phi_N + \Phi_D)/2$ ; difference between neutron and density porosity  $(\Phi_N - \Phi_D)$ ; and photoelectric effect (PE). Outputs are lithofacies occurrence probabilities.

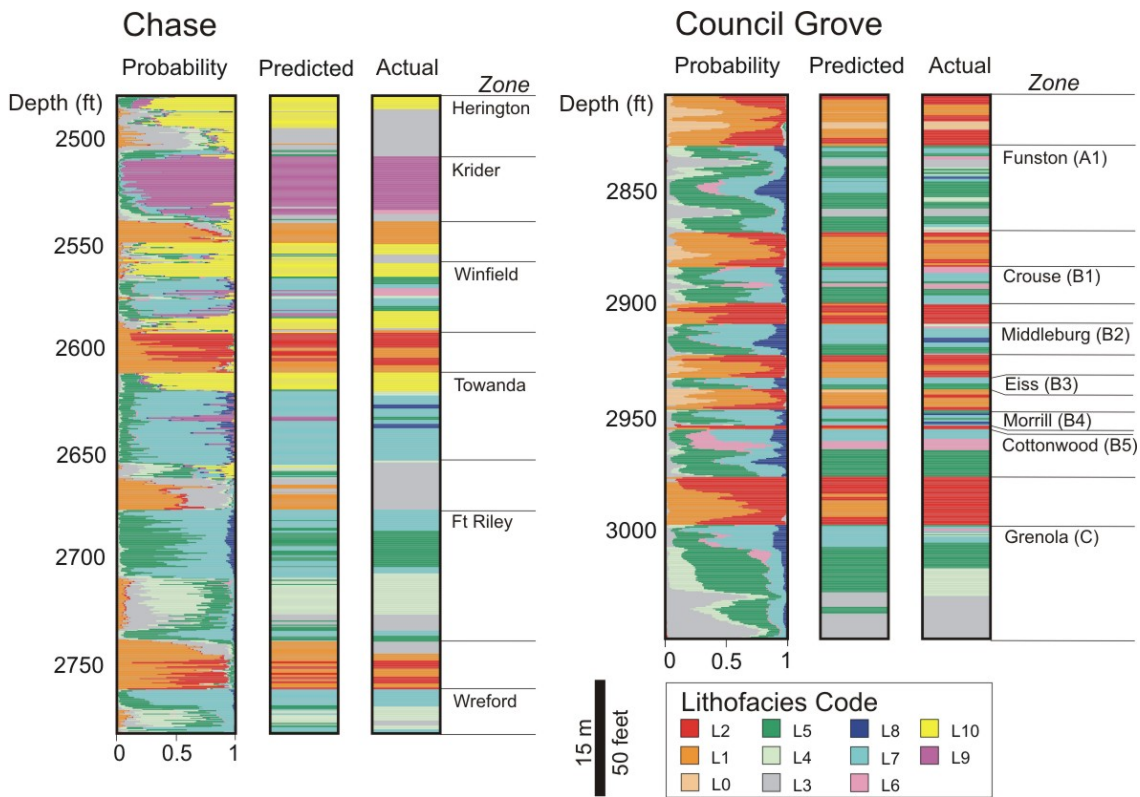


**Figure 6.5.** Comparison of predicted lithofacies versus core-defined lithofacies. Illustrated vertical plots of lithofacies membership probabilities, predicted discrete lithofacies (most probable), and lithofacies in core at the half-ft scale for the Chase and Council Grove from two separate wells in the training set (Youngren and Stuart, respectively). Neural networks were those utilized in estimating lithofacies in node wells (trained on all wells). Probabilities were not used as an input for modeling, but they do illuminate some of the misallocations (actual lithofacies is often in “second place”).

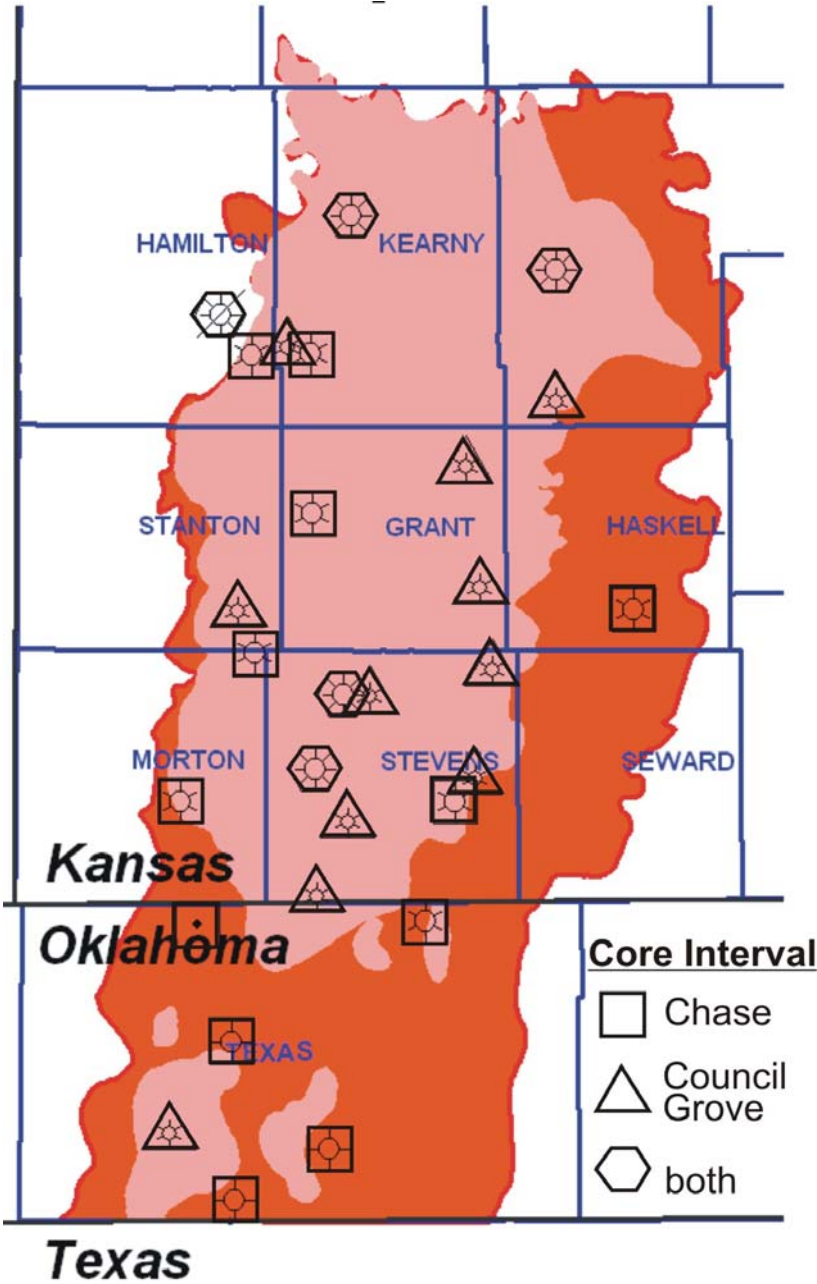


**Figure 6.6.** Distribution of Hugoton cores (continuous) for which lithofacies were defined at half-ft (0.15 m) intervals.

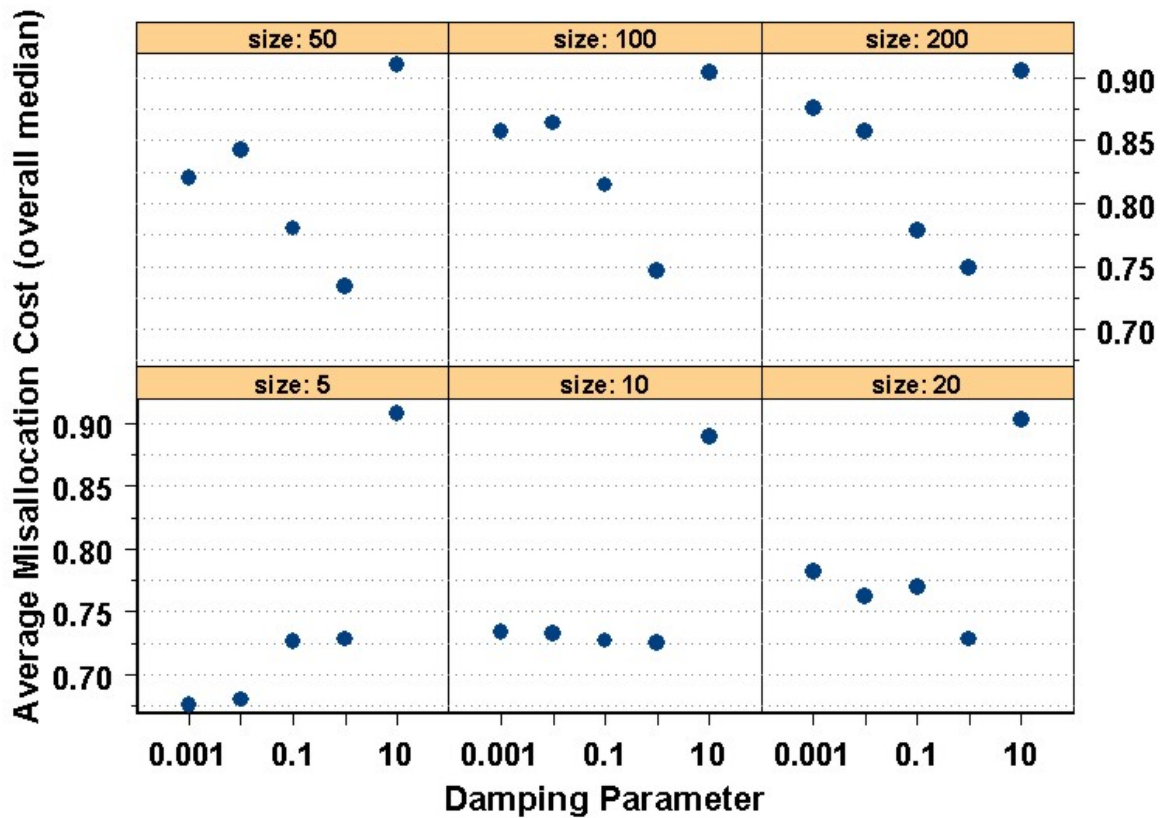


**Figure 6.7.** Example results for cross-validation analysis to determine optimal values of neural network size (number of hidden-layer nodes) and damping parameter. Results shown are the median over eight Council Grove wells with core-defined lithofacies and wireline photoelectric curve. The procedure was to perform five trials per well: leave out each well in turn, train on the other 7 wells, and predict on the subject well. Median average misallocation cost versus damping parameter and network size for all wells were then plotted. A network size of 20 hidden layer nodes and a damping parameter of 1.0 were chosen.

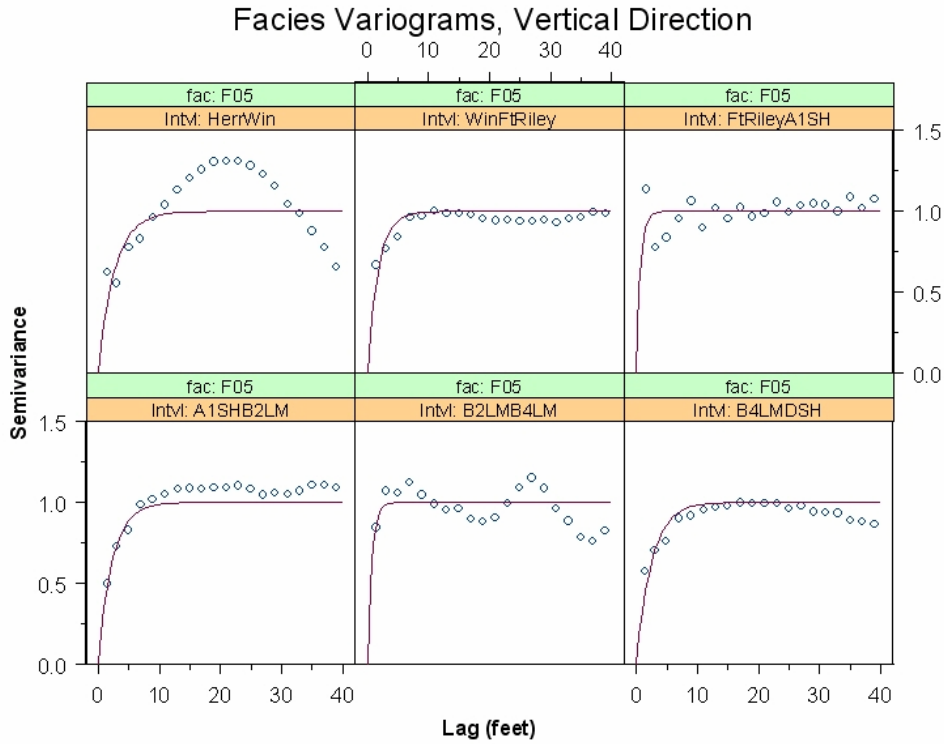


**Figure 6.8.** Empirical variograms (points) and fitted exponential models (lines) in the vertical direction for occurrence of facies 5 in all six submodels.

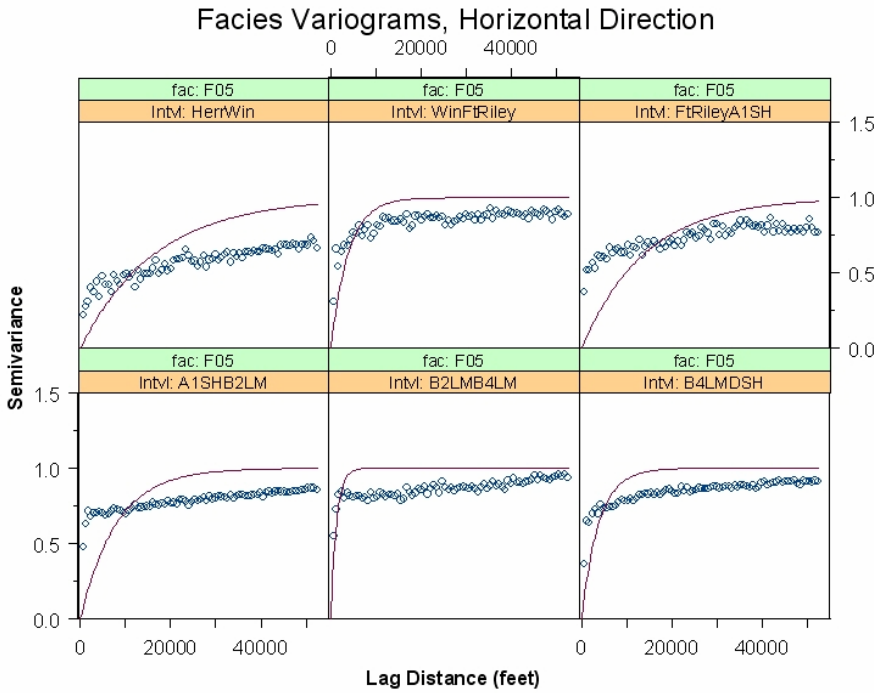


**Figure 6.9.** Empirical variograms (points) and fitted exponential models (lines) in the horizontal direction for occurrence of facies 5 in all six submodels.

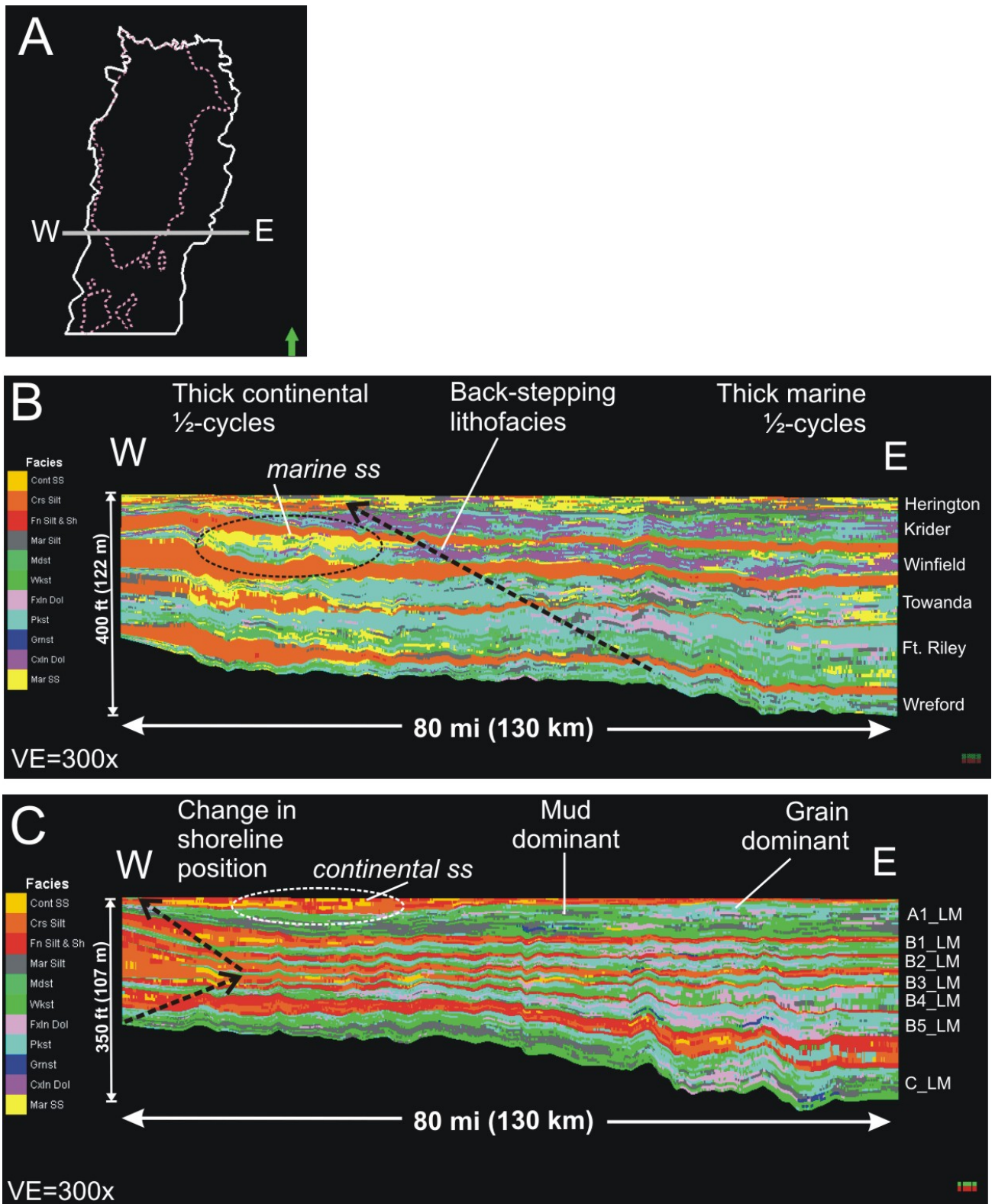
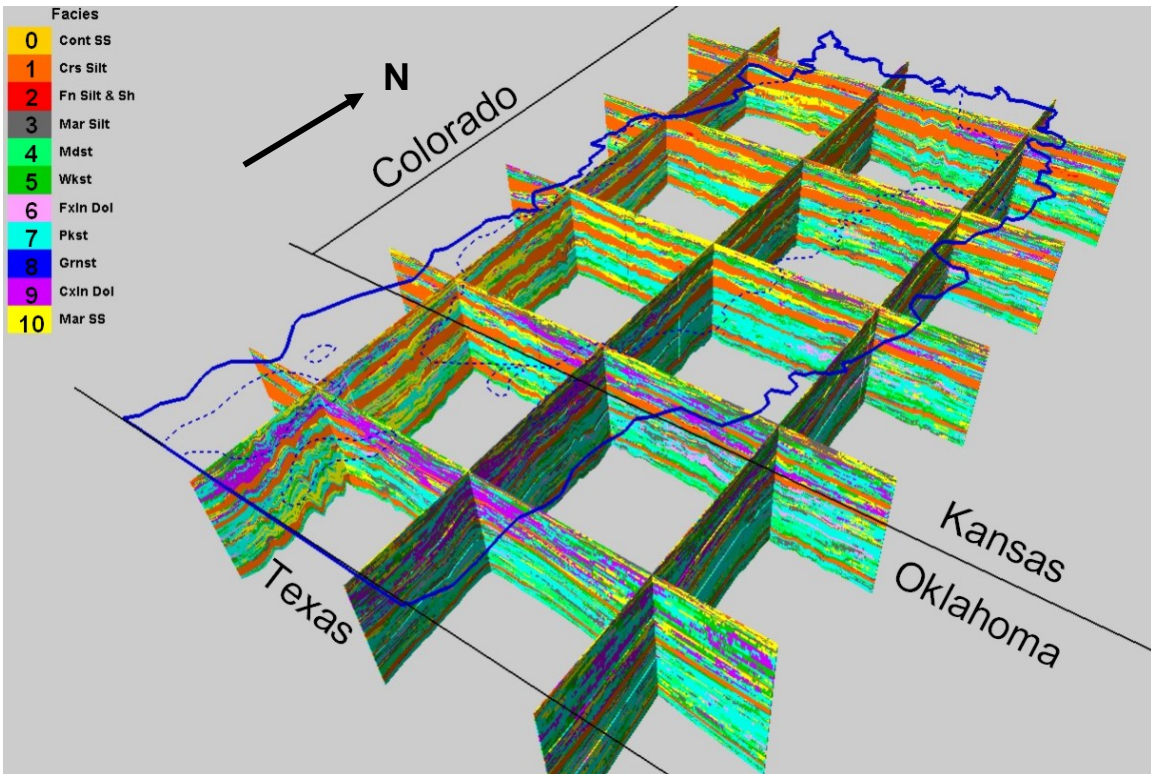
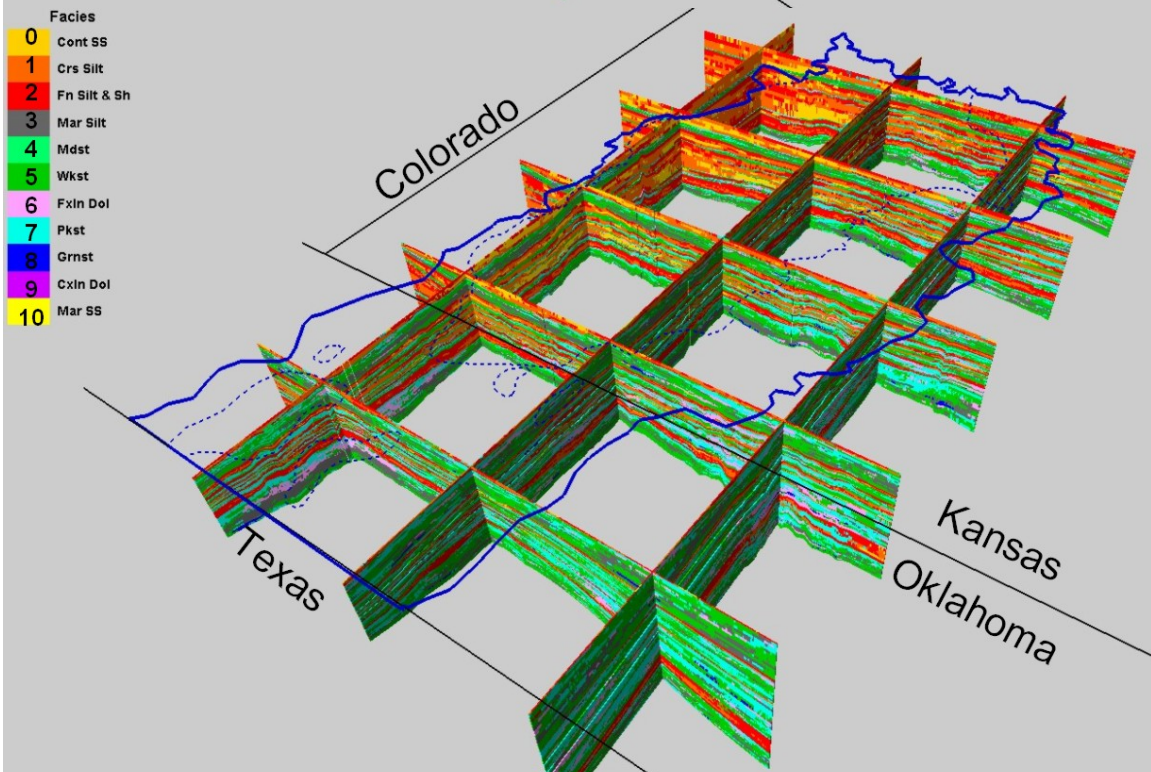


**Figure 6.10.** Lithofacies in stratigraphic cross sections across the Hugoton shelf **(A)** for the Chase **(B)** and Council Grove **(C)**. Cross sections are 10-15 degrees from being dip sections and are hung on the top of the Chase (B) and the Council Grove (C). Some

key observations can be made: 1) In both the Chase and Council Grove, continental half-cycles (yellow-orange to red lithofacies) are thickest at the west field margin and thin basinward (southeasterly). The pattern for the marine half-cycles is the opposite and, somewhat reciprocal, relationship with the continental half-cycles. 2) Back-stepping pattern in lithofacies distribution from one marine cycle to the next in the Chase. 3) Three Council Grove marine half-cycles “pinch out” near the west field margin, marking a paleo-shoreline that appears to then move northwesterly (landward) upsection. 4) Trend in carbonate rock texture from mud dominated (landward) to grain dominated (basinward), especially in the Council Grove. Large-scale sedimentation patterns and distribution of resultant lithofacies (at the cycle scale) are largely a function of the position on the shelf and reflect the interaction of shelf geometry, sea level, and possibly, the proximity to siliciclastic sources. Lithofacies distribution and cycle-stacking patterns at larger scales may be a function of higher-order cyclicity and a shift from icehouse to green house conditions (upward) during the Lower Permian. (*Model version: Geomod3*)



Chase Group



Council Grove Group

**Figure 6.11.** Stratigraphic cross section fence diagrams of the entire Hugoton cellular lithofacies model. View is from the southeast; datum is top of Chase and top of Council Grove; line spacing is 25 mi (40 km); vertical exaggeration = 200x. Continental siltstones (red and orange) separate the marine carbonate half-cycles, the main pay zones (cooler colors) prevail in the northwest, updip, landward portion of the model, while the marine carbonate dominates downdip (basinward). Both continental (yellow-orange) and marine sandstone (yellow) are most abundant landward.

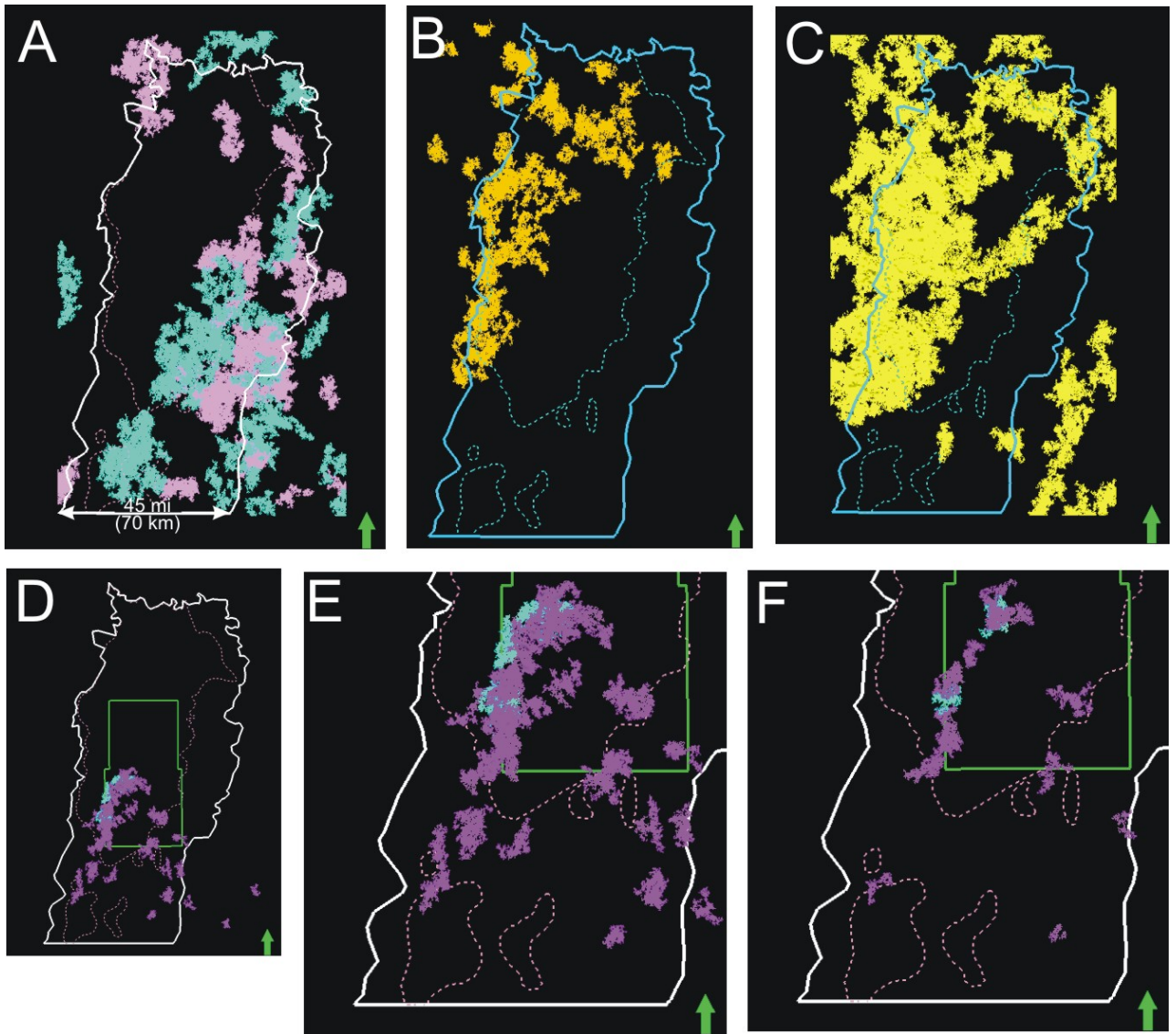


**Figure 6.12.** Maps showing lithofacies distribution of selected lithofacies. Illustrated are map views of “connected volumes” generated in Schlumberger’s Petrel™ modeling application. Connected volumes are collections of touching cells in the cellular model having common properties and, for this model, help to demonstrate the remarkable lateral continuity of flow units within the Wolfcamp. **(A)** Thirty largest connected volumes in the Crouse Limestone (B1\_LM) packstone, packstone-grainstone (L7, blue) and fine-crystalline dolomite (L6, pink) having porosity > 8%. **(B)** Fifteen largest connected volumes in the Speiser Shale (A1\_SH) continental sandstone (L0) with porosity > 12%. **(C)** Twenty largest connected volumes of marine sandstone (L10) having porosity > 15%. **(D)** Top 20 connected volumes for Krider packstone, packstone-grainstone (L7, blue) and coarse-crystalline dolomite (L9, purple) having porosity > 16%. **(E)** Enlarged area of D. **(F)** Same as E except for porosity > 18%. Grant and Stevens counties are outlined in green for reference in D through E. (Model version: Geomod 3)

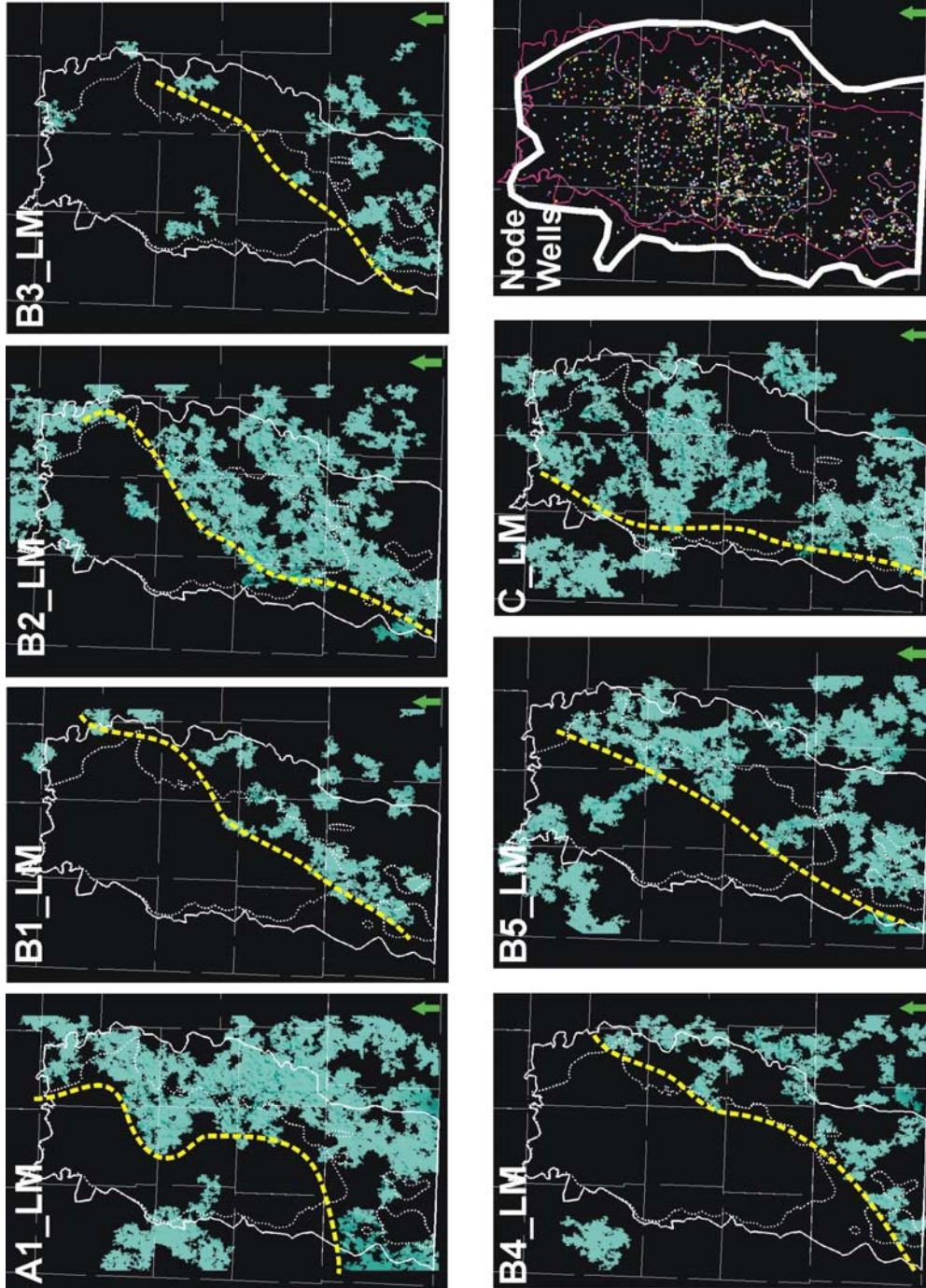


**Figure 6.13.** Distribution of packstone-grainstone lithofacies (L7) for Council Grove marine intervals. Illustrated are 2-D map views of the 15 largest connected 3-D volumes from the Hugoton cellular geo-model for L7 cells having greater than 10% porosity, except in the B5\_LM where 14% was the lower cutoff. Areas outside node well control may be ignored. Dashed line highlights the approximate updip limit for the larger grain-supported marine carbonate geobodies. (Model version Geomod 4).

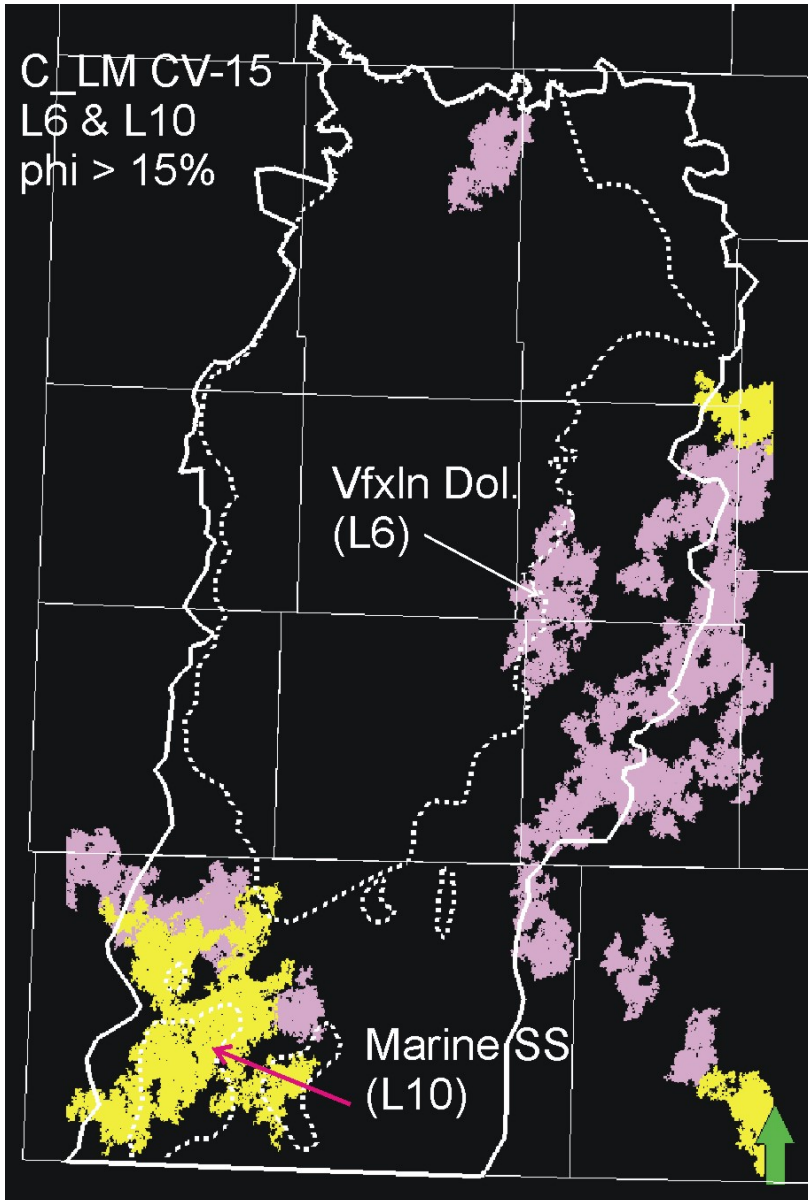


**Figure 6.14.** Distribution of marine sandstone (L10) and very fine-crystalline dolomite lithofacies (L6) in the Grenola (C\_LM) of the Council Grove. Illustrated are 2-D map views of the 15 largest connected 3-D volumes from the Hugoton cellular geo-model for L10 and L6 cells having >15% porosity. Marine sandstone is the productive lithofacies in the southwest portion of the model where this Council Grove zone has a distinctly different (Lower) FWL than Hugoton reservoir system (*Model version Geomod 4*).

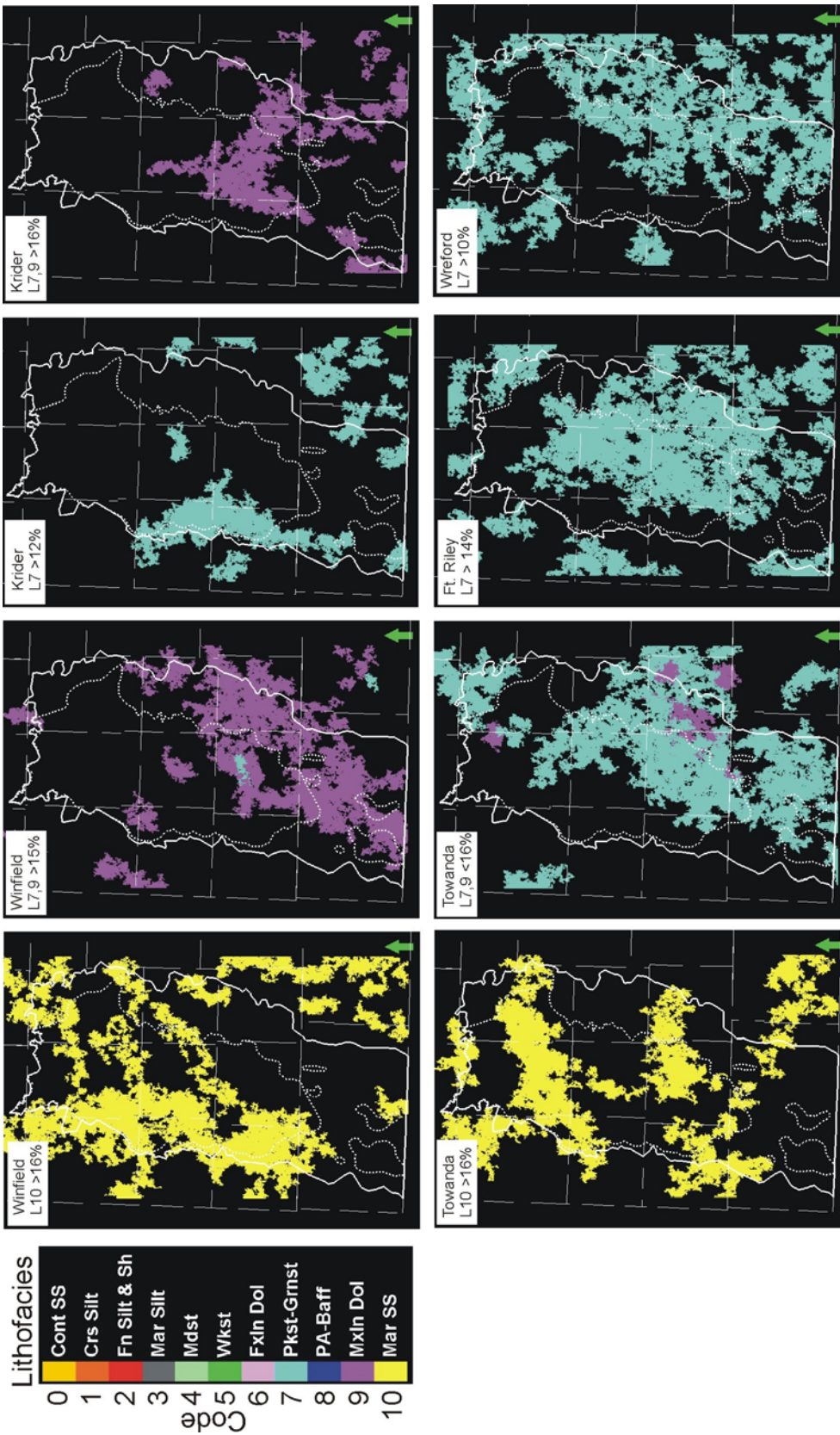


**Figure 6.15** Distribution of the main pay zone lithofacies for Chase Group marine half-cycles, in ascending stratigraphic order, counterclockwise starting in the lower right corner: Wireford, Towanda, Winfield and Krider. Herington is not shown. Where two lithofacies in a single half-cycle have significant occurrence two maps are shown for the same interval for comparison. (Model version Geomod 4)

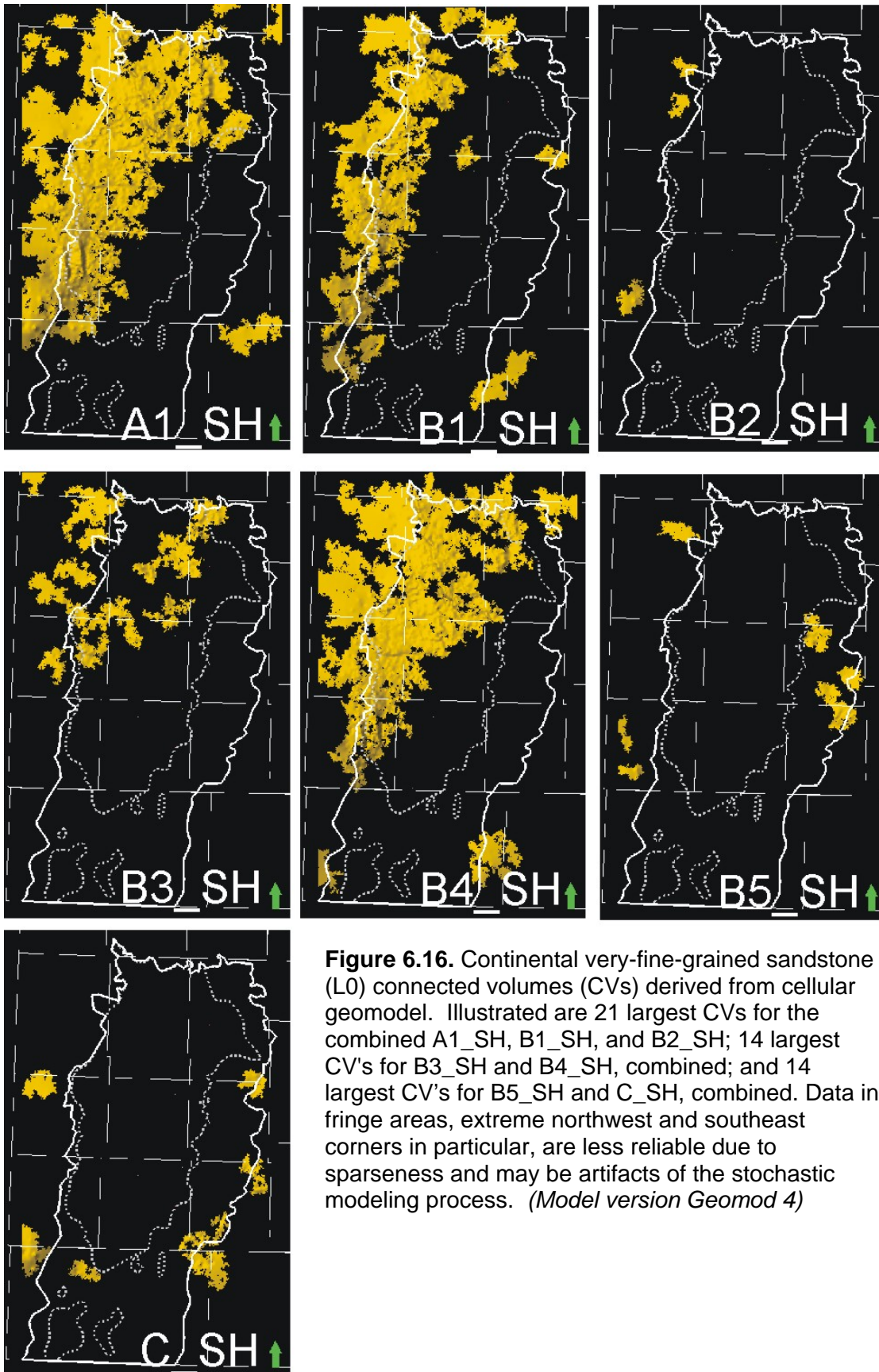


**Figure 6.16.** Continental very-fine-grained sandstone (L0) connected volumes (CVs) derived from cellular geomodel. Illustrated are 21 largest CVs for the combined A1\_SH, B1\_SH, and B2\_SH; 14 largest CV's for B3\_SH and B4\_SH, combined; and 14 largest CV's for B5\_SH and C\_SH, combined. Data in fringe areas, extreme northwest and southeast corners in particular, are less reliable due to sparseness and may be artifacts of the stochastic modeling process. (Model version Geomod 4)

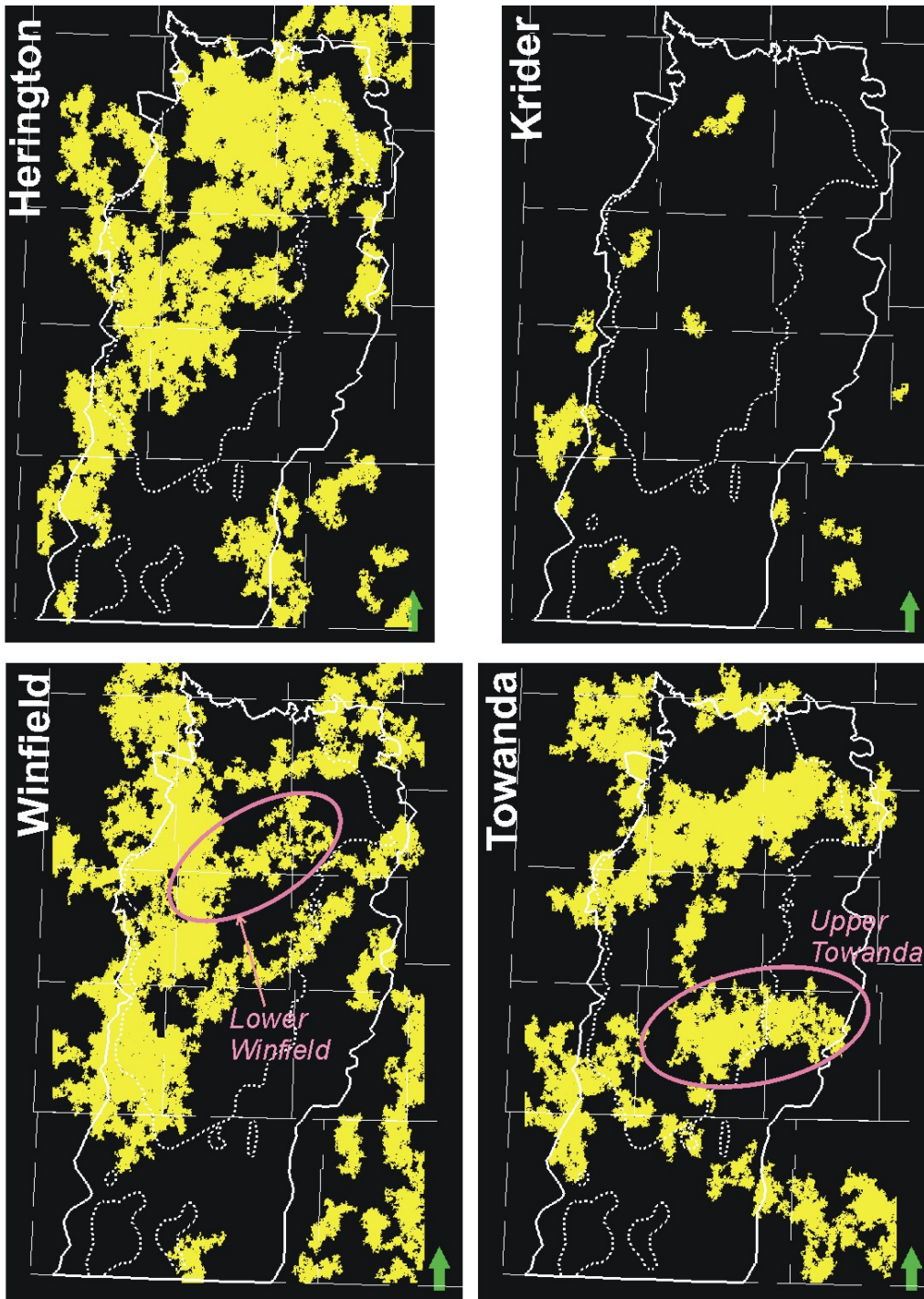


**Figure 6.17.** Marine fine-grained sandstone (L10) connected volumes (CVs) in the upper Chase, derived from cellular geomodel. Illustrated are the 15 largest connected volumes for the lithofacies cells having >16% porosity for the Krider, Winfield, and Towanda. A 14% porosity minimum was chosen for the Herington. Sandstone is prevalent throughout the entire Herington interval to the northwest, while it is mainly restricted to the upper portion of the Winfield except to the west (entire interval) and where otherwise noted. In the Towanda, sandstone tends to be distributed throughout the entire interval where it does occur, except where noted.

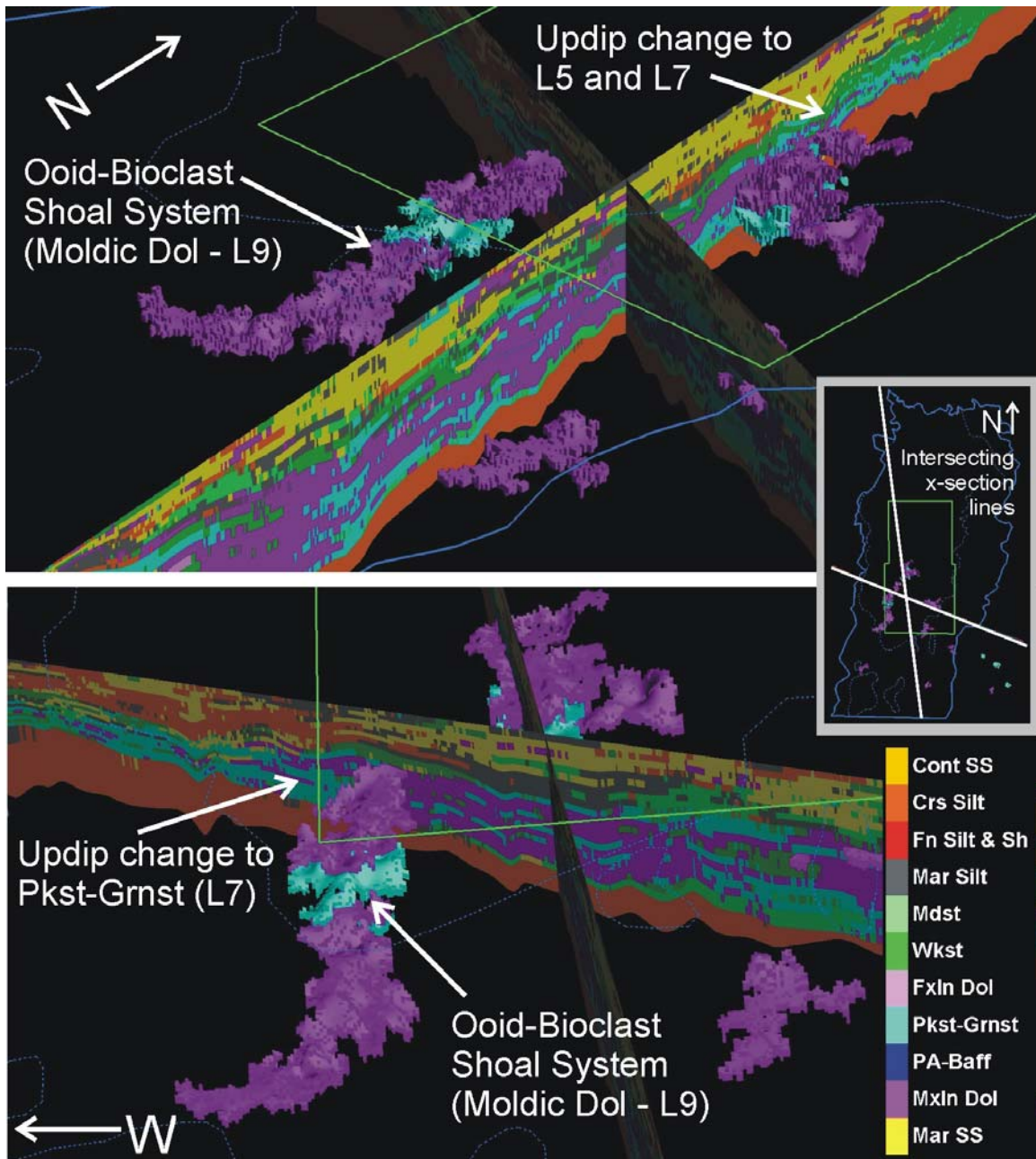


**Figure 6.18.** 3-D view of intersecting cross sections of Herington, Krider, and Odell intervals (upper Chase) and Krider connected volumes (CV's). CV's are for medium crystalline moldic dolomite (L9) and packstone (L7) having greater than 18% porosity (same as in Figure 6.12F). Cross sections' orientations are shown in the inset map. The main geobody (CV's) shown is an ooid-bioclust shoal defined in core in the Flower A1 core, Stevens County, Kansas. The shoal facies changes updip to the north to wackestone (L5) and packstone (L7), and to the west to L7, of poorer reservoir quality. (Model version: Geomd 3)

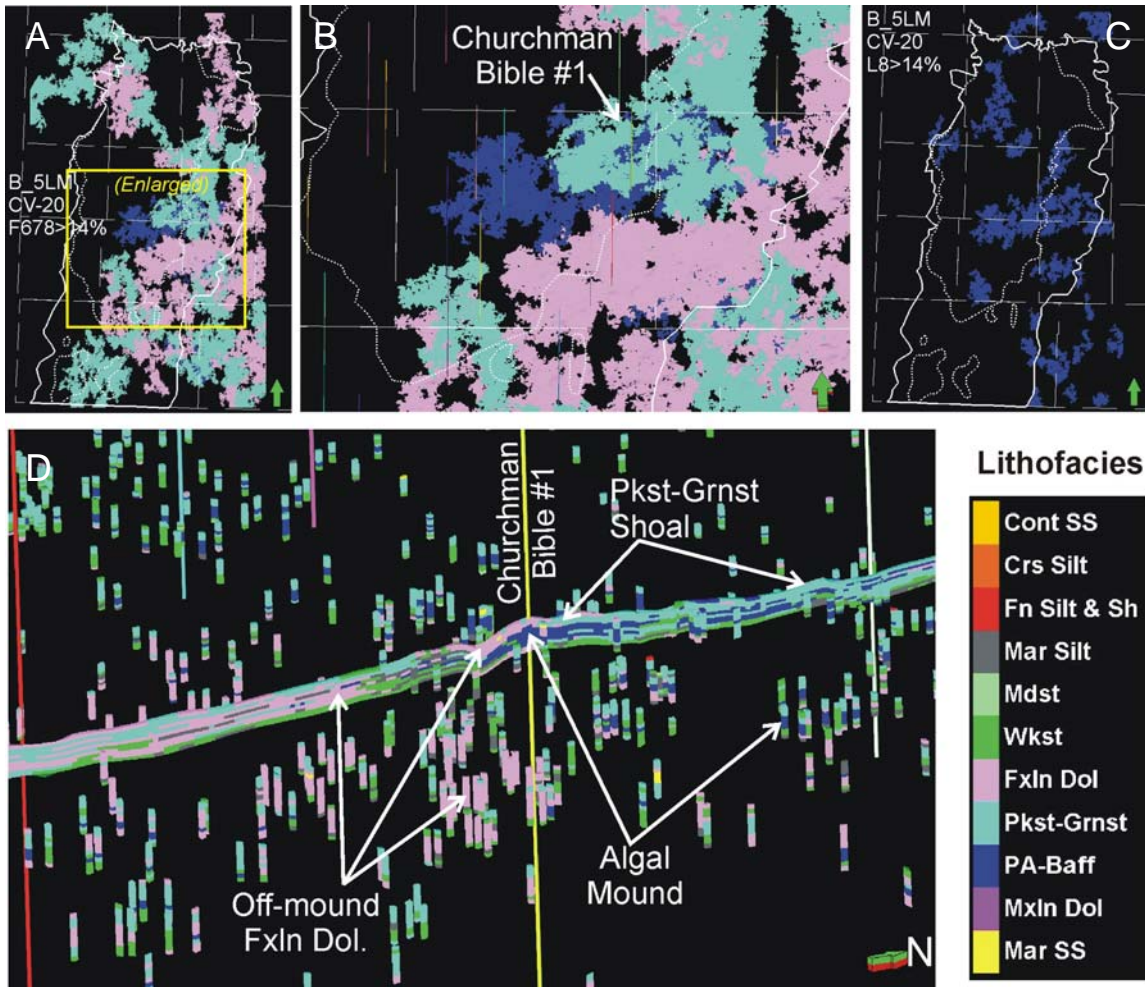


**Figure 6.19.** Connected volumes and 3-D view of Cottonwood (B5\_LM). **(A)** Twenty largest CV's for lithofacies very fine-crystalline dolomite (L6), packstone-grainstone (L7), and phylloid algal bafflestone (L8) having porosity > 14%. **(B)** Enlarged portion of (A). **(C)** Twenty largest CV's of L8, alone, having porosity > 14%. **(D)** 3-D view of a portion of the cellular model restricted to the Cottonwood. Cross section is oriented south-north and passes through a well with core, the Churchman-Bible, location shown in (B). Lithofacies blocked to node wells are also shown at all node wells in the area. What appear as a patchwork of lithofacies in the 2-D map views of 3-D CV's is actually overlapping discrete geobodies of three lithofacies.

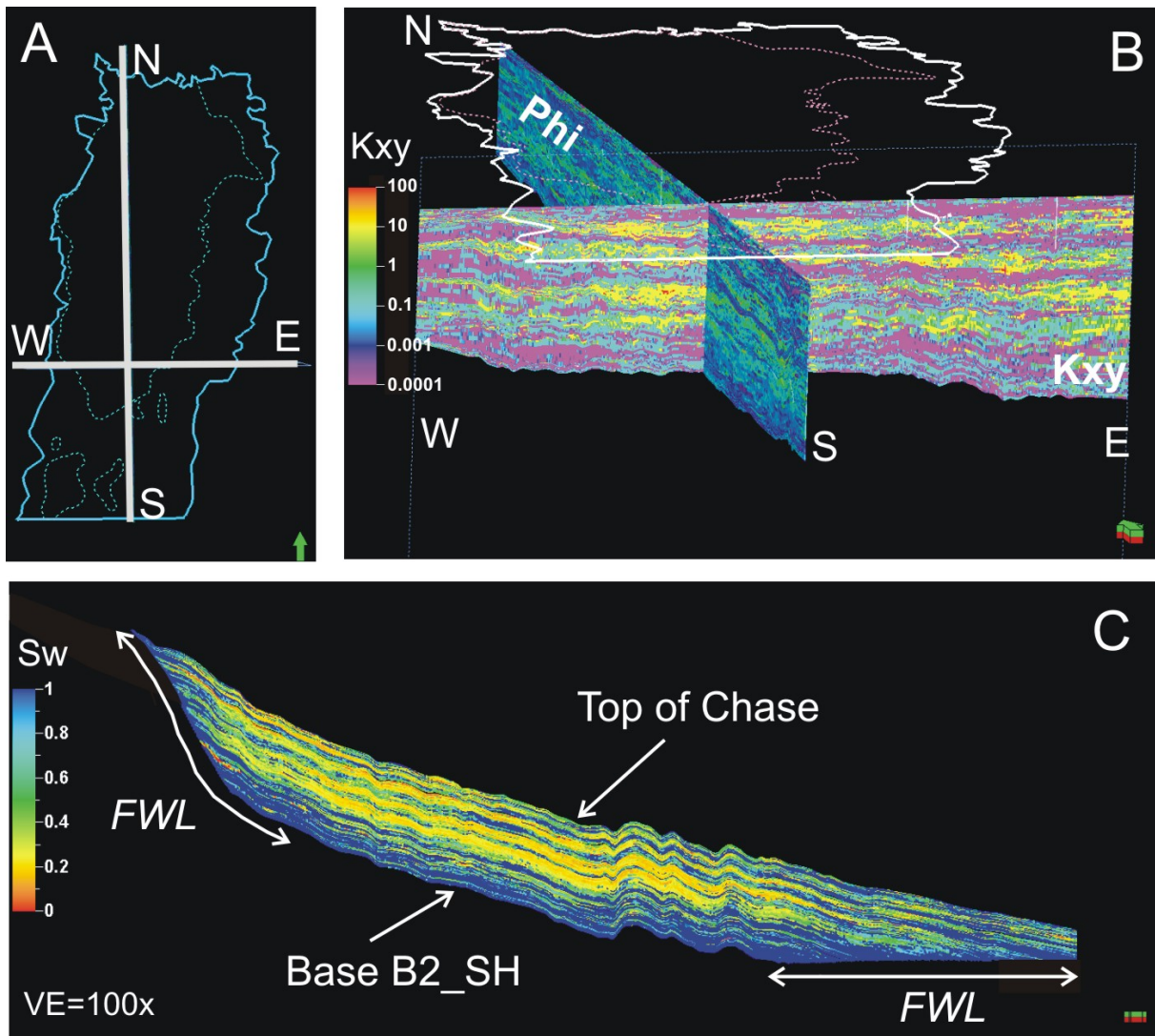


**Figure 6.20.** Property distribution in cellular Hugoton model in cross section. **(A)** Location of cross sections. **(B)** Chase group stratigraphic cross-section (datum is top of Chase). Horizontal permeability is shown in west-east section and porosity (0-30%, yellow is 22%) is in the north-south section. **(C)** Chase Group through Easley Creek Shale (B2\_SH, Council Grove) water saturation. Free water level is the base of the cross-section on the west and east side and the base of the Easley Creek (B2\_SH) in the middle where the FWL is lower in the stratigraphic column (not able to display all models simultaneously). FWL crosses stratigraphic boundaries in both updip and downdip positions. Highest permeability (Kxy) and porosity (Phi), and lowest water saturation (Sw) are found in marine carbonates and sandstones. Continental siltstones separating the marine carbonates are the intervals with Kxy and Phi, and higher Sw. (Model version: Geomod 3)

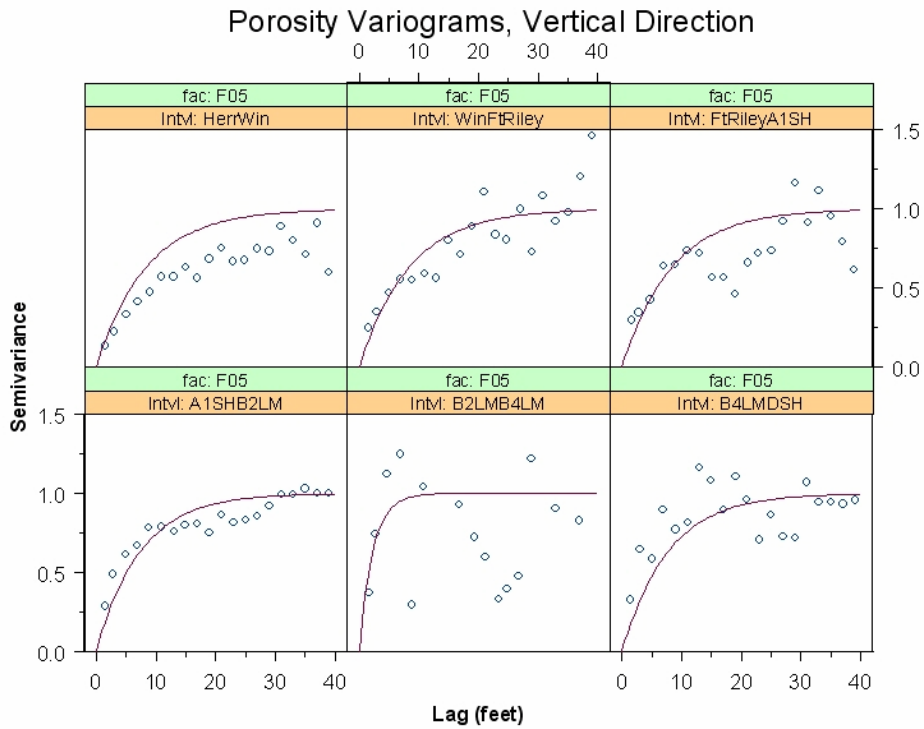


**Figure 6.21.** Empirical variograms (points) and fitted exponential models (lines) in the vertical direction for porosity in facies 5 in all six submodels.

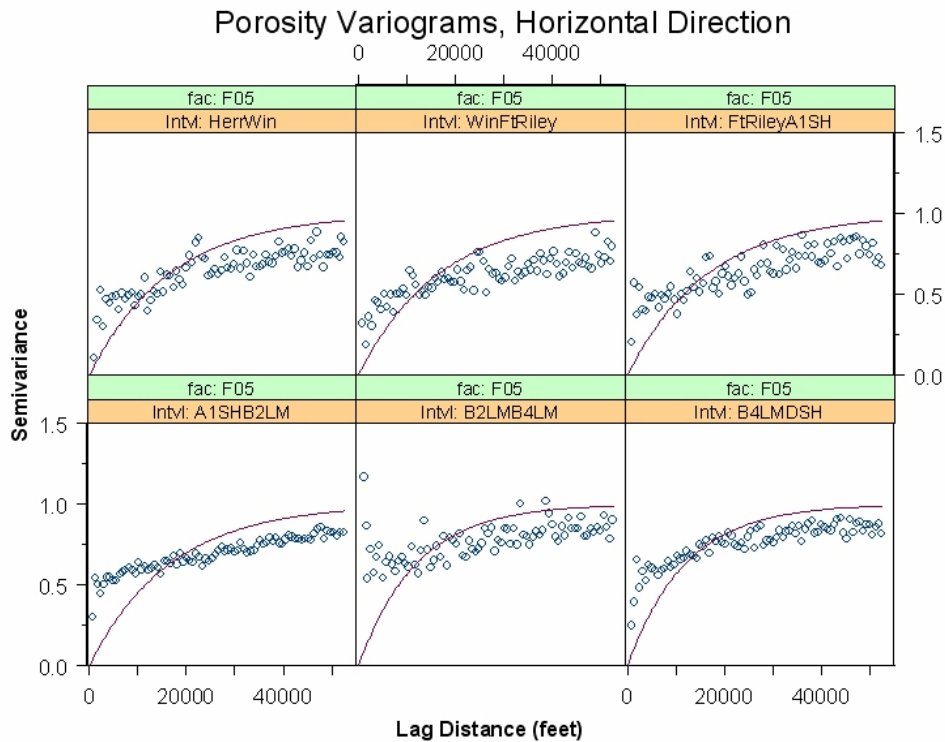


**Figure 6.22.** Empirical variograms (points) and fitted exponential models (lines) in the horizontal direction for porosity in facies 5 in all six submodels.

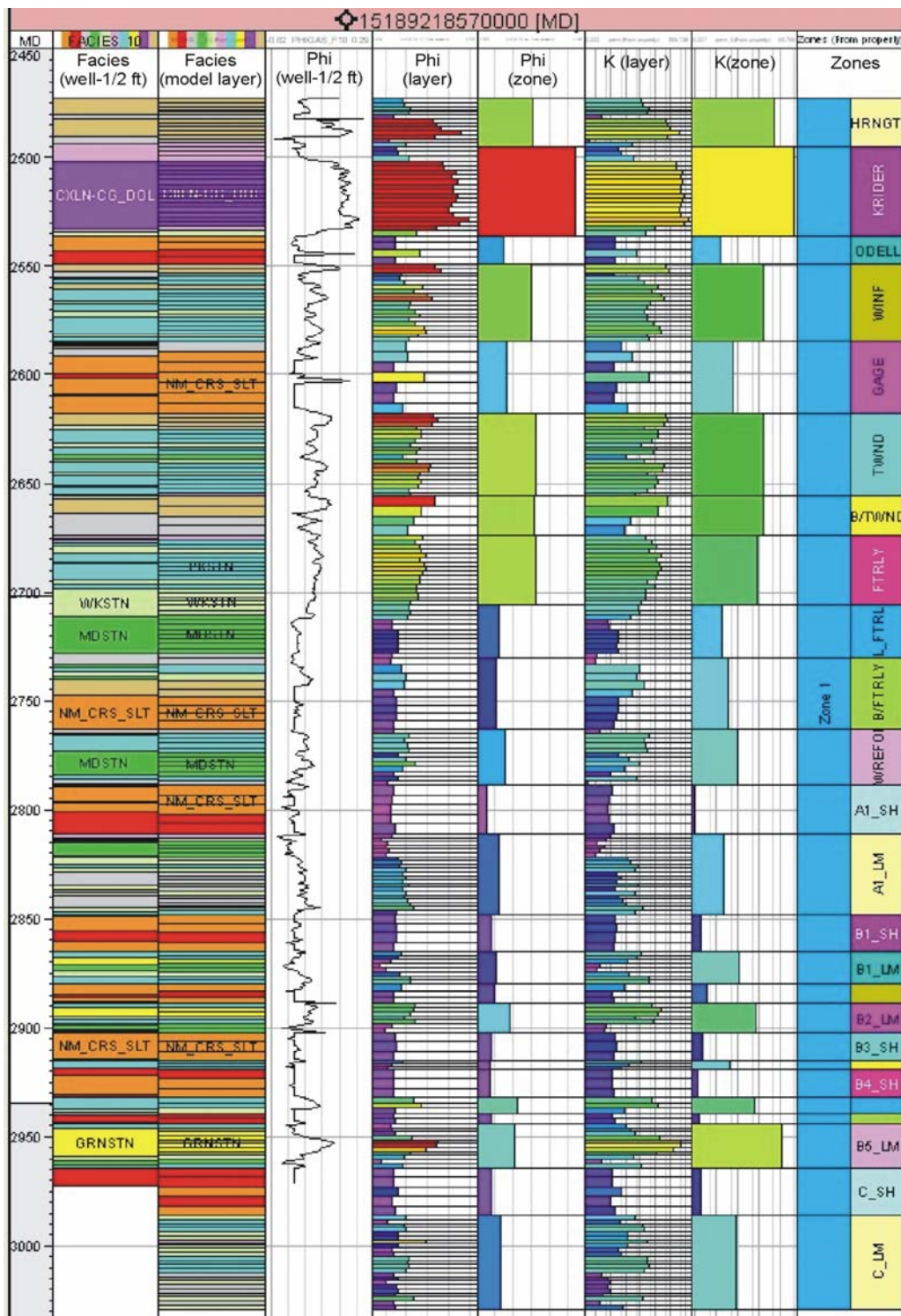


**Figure 6.23.** Lithofacies and layers for Flower A-1 well. Initial 998 half-ft layers were upscaled to 209 layers ranging from 2 ft to 4 ft thick. Geomodel permeability was calculated for the average porosity of the each of the 209 layers and the principal lithofacies. The 209 layers were upscaled to 25 zones for reservoir simulation (Chapter 9).

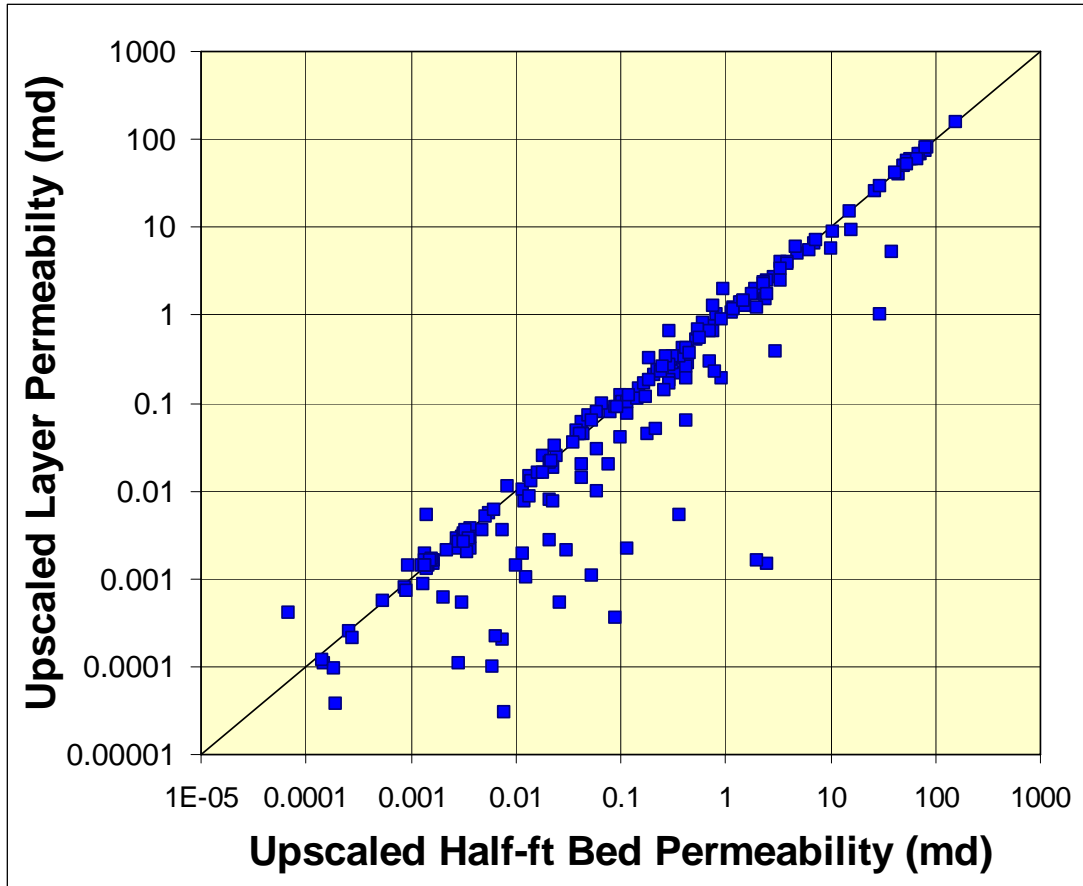


**Figure 6.24.** Crossplot of upscaled layer permeability versus upscaled half-ft bed permeability for 209 layers in the Flower A-1 well. Layer permeabilities were calculated from average layer porosity and lithofacies. Upscaled half-foot bed permeabilities represent arithmetic average of permeability for all half-foot beds within the layer. Differences between the upscaling methods result from the presence of thin, higher-permeability intervals in layers and differences in averaging porosity and permeability.

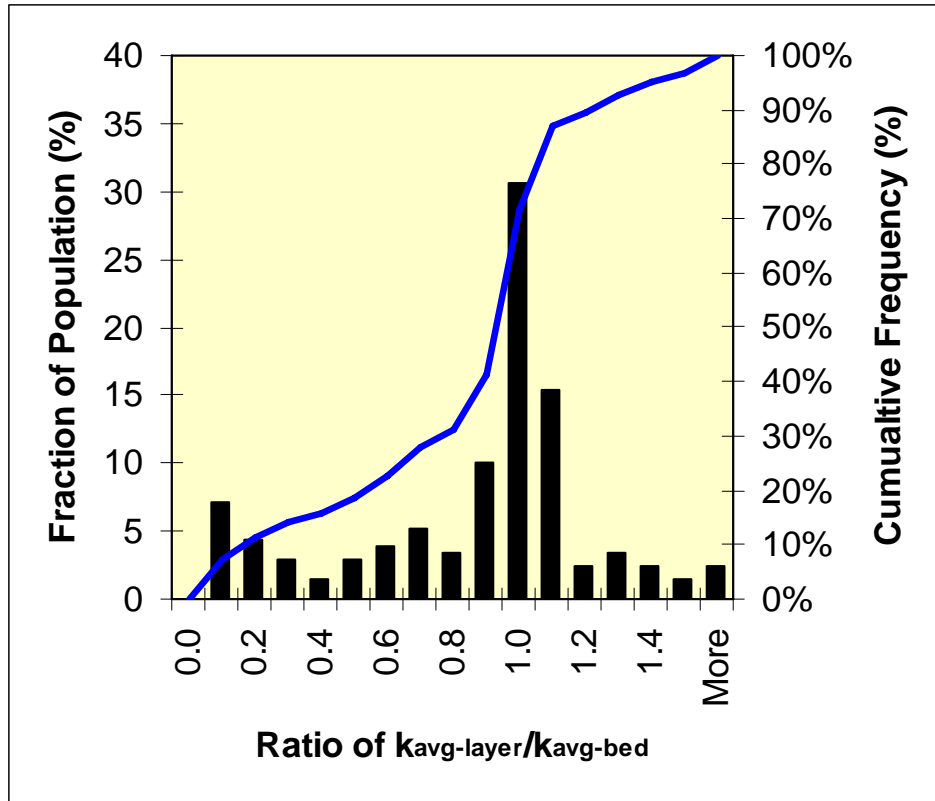


**Figure 6.25.** Frequency distribution of ratio of layer permeability ( $k_{avg-layer}$ ) to bed permeability ( $k_{avg-bed}$ ) showing ~75% of layers exhibited permeabilities with 40% of half-ft bed average permeability. The ratio is skewed to lower values as discussed in text.

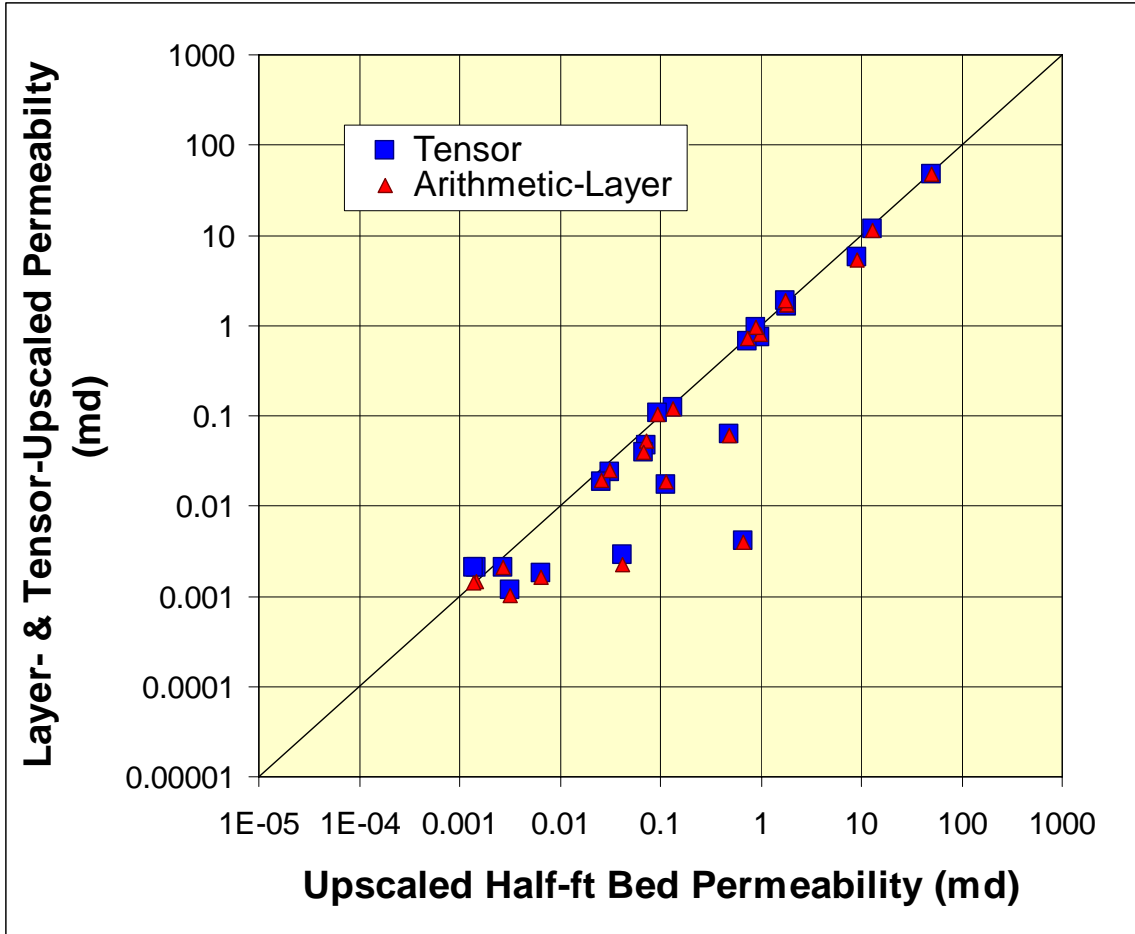


**Figure 6.26.** Crossplot of layer- and PSK-solver tensor-upscaled zone permeabilities versus half-ft bed upscaled zone permeabilities. This figure shows that both layer- and tensor-upscaled zone permeabilities agree with bed permeabilities with  $80 \pm 30\%$  except for a few significant outliers. The five zones exhibiting significantly higher bed permeabilities all have thin, high-permeability beds in one or two layers.